Materials Advances

ROYAL SOCIETY OF CHEMISTRY

PAPER

View Article Online
View Journal

Cite this: DOI: 10.1039/d6ma00143b

Ternary $Ag{\cdot}Eu_2O_3{\cdot}SrCO_3$ nanomaterials for enhanced photocatalytic performance of CV dye and efficient nitrite sensor development

Shubrojit Dey,[a] Md Abdus Subhan,[a]†* Umer Shahzad,[b] Mohammad Al-Mamun,[c] Didar Hossain,[d] Maha G. Batterjee,[e] Abul Kalam Azad,[d] O. Madkhali,[f] Khalid A. Alzahrani[bg] and Mohammed Muzibur Rahman[bg]*

Ternary $Ag{\cdot}Eu_2O_3{\cdot}SrCO_3$ nanomaterials (NMs) were developed using a facile co-precipitation process. XRD, SEM, EDS, FTIR, PL, and Raman spectroscopy were used to characterize the NMs. The XRD pattern showed an average particle size of 53.62 nm and good crystallinity. The photocatalytic activity of crystal violet (CV) dye was assessed using several variables, including pH, reusability, and varying concentrations of NMs in visible light. The NM dose of 0.06 g in basic medium exhibited the best dye removal efficiency of 97.7%. Both Gram-positive and Gram-negative pathogenic bacteria were suppressed by the NMs. This paper reports on the fabrication of an efficient and sensitive nitrite sensor in the aqueous phase using $Ag{\cdot}Eu_2O_3{\cdot}SrCO_3$ NMs, and a constructed glassy carbon electrode (GCE) using 5% Nafion. The fabricated nitrite sensor exhibited a linear relationship between the oxidation peak current and nitrite concentration over a wide concentration range of 0.15 to 50.0 μM, which is the linear dynamic range (LDR). The detection limit (LOD) and sensitivity were calculated as 0.61 μM (S/N = 3) and 27.4261 μA μM^{-1} cm^{-2}, respectively. The detection of nitrite was not affected by common interfering ions. The $Ag{\cdot}Eu_2O_3{\cdot}SrCO_3$/Nafion/GCE sensor was able to identify nitrite in natural samples. The newly reconfigured Nafion/GCE that used $Ag{\cdot}Eu_2O_3{\cdot}SrCO_3$ NMs exhibited high repeatability, reproducibility, selectivity, sensitivity, and long-term stability toward nitrite. It introduced a new ternary nanostructure material for the efficient detection of environmental contaminants, as well as functioning as an efficient photocatalyst for environmental and ecological protection on a broad scale.

Received 31st January 2026,
Accepted 21st March 2026

DOI: 10.1039/d6ma00143b

rsc.li/materials-advances

Introduction

The release of organic dye pollutants into natural water sources has made it very difficult to provide clean water to a large percentage of the population. As the population increases, subterranean water will not be enough to meet everyone's water needs.[1] Different types of dyes are used for different purposes, such as coloring agents in food industries, cosmetics and personal care, pharmaceutical industries, biological research, paint and paper industries, photography industries, indicators and sensors, and, most widely, textile industries for coloring fabrics.[2–8] The textile processing industry frequently uses one of the dyes, CV, an organic chloride salt, and triphenylmethane dye, which is also utilized as a biomedical stain and disinfectant. Despite its widespread use, CV is carcinogenic to humans and remains in industrial effluents for a long time.[9] As a result, scientists from all over the world have concentrated on creating and enhancing new technologies and a more efficient approach to wastewater treatment. An environmentally acceptable and sustainable solution to energy and environmental issues is provided by nano-photocatalytic technology.[10] Semiconductor metal oxide photocatalysis is one such technique that has received a lot of attention lately because of its potential uses in environmental cleanup.[11,12]

[a] Department of Chemistry, School of Physical Sciences, Shahjalal University of Science and Technology, Sylhet-3114, Bangladesh. E-mail: subhan-che@sust.edu
[b] Chemistry Department, Faculty of Science, King Abdulaziz University, Jeddah 21589, Saudi Arabia
[c] Centre for Clean Environment and Energy, Griffith School of Environment, Griffith University, Gold Coast Campus, QLD 4222, Australia
[d] Department of Genetic Engineering & Biotechnology, Shahjalal University of Science and Technology, Sylhet-3114, Bangladesh
[e] Department of Chemistry, College of Sciences & Arts, King Abdulaziz University, Rabigh, Saudi Arabia
[f] Department of Physical Sciences, Physics Division, College of Science, Jazan University, P.O. Box 2097, 45142 Jazan, Saudi Arabia
[g] Center of Excellence for Advanced Materials Research, King Abdulaziz University, Jeddah 21589, Saudi Arabia. E-mail: mmrahman@kau.edu.sa; Tel: +966596421830
† Current affiliation: Texas Tech University, Lubbock, Texas 79409, USA.

The usage of nano mixed metal oxides in data storage devices is supported by their strong ferromagnetic characteristics and high Curie temperature. When it comes to detecting and identifying dangerous and explosive gases, semiconductor metal oxides' optical, electrical, and thermal characteristics truly stand out. There are two types of semiconductor metal oxides: n-type and p-type. Metal oxides can form semiconductors because of their broad band gaps.[13] Due to their large surface area, silver nanoparticles (NPs) exhibit a variety of characteristics and uses.

The surface plasmon resonance (SPR) of Ag NPs increases the photoabsorption capacity in Ag@ZnO.[14] Furthermore, Ag NPs increase absorption, help produce reactive oxygen species (ROS), and inhibit the recombination of photoinduced electron–hole pairs by trapping electrons in Ag–TiO_2/porous glass (PG), all of which contribute to the composite's exceptional photocatalytic activity.[15] The broad-spectrum and strong antibacterial capabilities of Ag NPs make them a promising solution to this problem.[16]

Eu_2O_3 has a wide band gap of 4.3 $\pm$ 0.2 eV.[17] Eu_2O_3 will increase lattice stress and cause crystal defects to occur if a dopant or second metal is added, turning the material into an excellent semiconductor. It is an effective insulator when in the form of pure Eu_2O_3. It serves as a metal–insulator–metal (MIM) capacitor.[18] The transesterification process is catalyzed by Eu_2O_3/Al_2O_3.[19] The unoccupied 4f state of Eu and the availability of valence electrons in Eu_2O_3 result in excellent photocatalytic activity in doped, binary, and ternary heterojunction metal oxide nanocomposites.[20–22]

$SrCO_3$, with a wide band gap of 3.17 eV, is useful as a capping agent for NPs. It also serves as a nanocarrier for drug delivery and targeted cancer therapy.[23,24] When $SrCO_3$ is combined with other semiconductors, its photocatalytic activity increases.[25] ZnO–$SrCO_3$ semiconductor-based composites degraded methylene blue (MB) under both UV and visible light irradiation.[26]

An antimicrobial agent either eliminates or inhibits the growth of microorganisms such as bacteria, fungi, and protozoa. In several industries, including water sanitization, materials, packaging, development, pharmaceuticals, and food, antimicrobial agents are essential. Metal oxide NMs are superior in antimicrobial applications. Different kinds of bacterial death mechanisms have been identified. However, the production of ROS is linked to the majority of the bacterial killing activity. Additionally, metal oxide NMs' physicochemical characteristics, such as compound production, particle size, surface, shape, dissolvability, and ROS generation, help them exhibit excellent antibacterial activity.[27] Also, ROS can degrade dye during photocatalysis. The semiconductor metal oxides can generate $^{\bullet}O_2^-$, and $^{\bullet}OH$ radicals during photoexcitation from oxygen and H_2O, respectively. These ROS are responsible for both dye degradation and bacterial killing ability.[28]

We developed a unique metal oxide nanocomposite, Ag·Eu_2O_3·$SrCO_3$, for multifunctional applications addressed in the current study because of the several significant applications of Ag, Eu_2O_3, and $SrCO_3$ NPs described above. In this study, we synthesized Ag·Eu_2O_3·$SrCO_3$ NMs using a simple co-precipitation method to investigate their photocatalytic characteristics using CV as a model dye, and antibacterial activities. Several techniques were used to examine the structural and morphological properties of the Ag·Eu_2O_3·$SrCO_3$ NMs. The photocatalytic activity of Ag·Eu_2O_3·$SrCO_3$ NMs was evaluated in a neutral, basic, and acidic medium. Furthermore, the antibacterial activity of the NMs was studied to look at how they affected both Gram-positive and Gram-negative bacteria.

Nitrite (NO_2^-) is an inorganic nitrogenous ion that is used in the nitrogen cycle, which is an important biogeochemical process that is essential in supporting life. It is a compound that is present in the environment and is currently used in numerous applications, specifically in the food industry and in the medical sector.[29] As a food preservative, NO_2^- is used in several products, especially in specific fish and meat products, naturally found in fruits and vegetables, and as a medication.[30] It is worth noting that nitrite is an important intermediate in generating nitrosamines, as well as in the biological production of nitric oxide (NO), which is a strong vasodilator and used as cardiac or kidney medicine.[31] Nitrite has a high solubility, and thus, it easily dissolves and permeates the soil, where it may be absorbed by plants and consumed by animals, hence entering the food chain and thus potentially causing risks to human and ecological health.[32] Moreover, the extensive use of nitrogen-based fertilizers contributes to pollution of the environment, specifically in the aquatic environment, where nitrite can contaminate groundwater and lower the quality of water.[33] There is a strong relationship between such contamination and serious health risks to humans, with endocrine disruption,[34] esophagitis, and even gastric cancer,[35] associated with the changes that occur when nitrite is converted into *N*-nitrosamines in the stomach.[36] Moreover, nitrite can react with haemolytic protein, hemoglobin, and cause a disorder to its capacity to carry oxygen in blood.[37–39] Therefore, the regulatory authorities have set strict levels of nitrite in drinking water. The recommended upper limit of concentration set by the World Health Organization (WHO) to protect the environment and human health against its adverse effects is about 3 mg L^{-1}.[40] Considering these dangers, it has become a pressing requirement to monitor nitrite concentration in samples of water regularly.[41]

This is because checking the nitrite content of food and drinking water is pivotal in protecting human health as well as environmental conservation. Rapid, accurate, and reliable methods of detecting nitrite must be developed. Existing detection techniques are chemiluminescence,[42] chromatography,[43] and spectrophotometry.[44] Nevertheless, these methods may also be characterized by significant limitations, including the utilization of dangerous substances and reagents, costly and complicated equipment, a high intensity of sample preparation, low selectivity, or the inability to conduct monitoring in the field.

Electrochemical sensors represent a potential solution since they are fast, sensitive, economical, and may be miniaturized.[45–49] These sensors can be fabricated in the form

of a portable device, and hence non-experts can carry out on-site nitrite analysis. Regardless of their merits, there are still some problems in improving the sensitivity and the general performance of the electrochemical sensors.

Use of a Ag·Eu_2O_3·$SrCO_3$ NM-modified glassy carbon electrode (GCE) is a superior method of sensing nitrite using linear sweeping voltammetry (LSV). Addition of silver (Ag), europium (Eu), and strontium (Sr) oxides improves the electrocatalytic characteristics of the electrode, which promotes better transfer of electrons and reduces the oxidation potential of the nitrite ions on the electrode surface. This change results in a significant enhancement in sensitivity and selectivity for nitrite and could be a viable candidate for environmental and food safety monitoring. Over the last couple of years, it has been proven that a metal oxide-based composite is an effective electrochemical sensor for nitrite.[50]

The utilization of an electrochemical sensor, which uses Ag, Eu, and Sr oxides, offers a simple means of determining nitrite concentration in water samples. The electrocatalytic behavior of the Ag·Eu_2O_3·$SrCO_3$/Nafion/GCE in the oxidation of nitrite was studied by employing both the cyclic voltammetry and linear sweep voltammetry methods. This paper will compare the functionalization of the newly synthesized nanocomposite to that of the individual NMs and will also optimize pH conditions and determine the variations in oxidation potential. To determine the reliability and consistency of the sensor, the sensor performance was also tested on interference, repeatability, and reproducibility to test its consistency.

Experimental section

Materials

Silver nitrate, $AgNO_3$ (Smart-Lab, Indonesia), europium(III) acetate hydrate, $Eu(CH_3CO_2)_3{\cdot}xH_2O$ (Sigma-Aldrich), strontium chloride hexahydrate, $Cl_2Sr{\cdot}6H_2O$ (Sigma-Aldrich), and sodium carbonate, Na_2CO_3 (Smart-Lab, Indonesia) were used for synthesizing NMs. For studying the photocatalytic activity, crystal violet (CV), $C_{25}H_{30}N_3Cl$ (Smart-Lab, Indonesia) dye was chosen. The hydroxyl radical was detected during photocatalysis by using sodium hydroxide, NaOH (Merck, Germany), and terephthalic acid, $C_8H_6O_4$ (Tokyo Chemical Industry CO., Ltd, >99.0%). Buffer capsules (pH 4, 7, and 9.2) (Smart-Lab, Indonesia) were used for the pH effect study.

Characterization techniques

The identification of composition, bulk crystal phase, and other relevant structural evidence of the materials studied in this work was characterized by X-ray diffraction (XRD, Bruker D8 Advance diffractometer, equipped with a graphite monochromator). The diffraction patterns were registered in the step scan method at 0.05 steps and at a measurement rate of 10 s per step. The diffraction patterns were recorded within the 2θ angle ranging from 20° to 80°. Scanning electron microscopy (SEM, JEOL JSM-7100F) was used for the morphology observation. Elemental analysis was carried out using an X-ray energy dispersive spectrometer (EDS) (Oxford Instrument) equipped with the HF-5000. Using a Renishaw inVia Raman Microscope with a 785 nm laser, 20× objective, and 100× objective, Raman spectroscopy was carried out. To guarantee that the exhibited spectra were typical, five measurements were taken for each sample. Peak fitting and background correction were performed using Renishaw Wire 5.0 software. A double beam UV-visible spectrophotometer (UV-1800 Series, UV-Vis spectrophotometer, Shimadzu Corporation, Kyoto, Japan), pH meter (model HI210 pH Meter, Hanna instruments, Romania), centrifuge machine (IEC SPINETTE centrifuge. DAMON/IEC Division), magnetic stirrer (Stuart Scientific), FTIR spectrophotometer (Shimadzu, IRPrestige-21), spectrofluorophotometer (Shimadzu Crop. Model RF-5301), electric muffle furnace (Gallenkamp, Korea), sonicator (GT SONIC-P2), and four digit electronics balance (Shimadzu) were used in this work.

Preparation of Ag·Eu_2O_3·$SrCO_3$ NMs

Standard co-precipitation of corresponding carbonates from the aqueous solution of the metal salts produced the NMs, Ag·Eu_2O_3·$SrCO_3$. First, distilled water (DW) was used to prepare

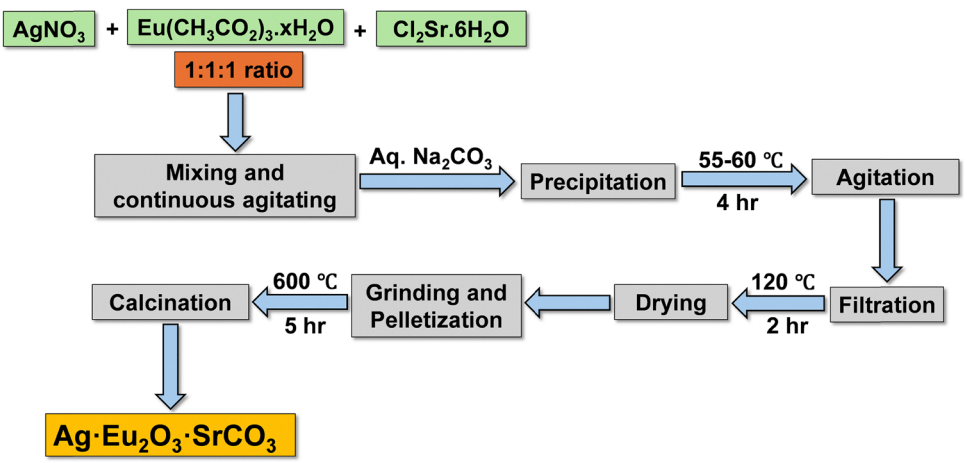

Scheme 1 Synthesis of Ag·Eu_2O_3·$SrCO_3$ NMs using a co-precipitation method.

solutions of (0.25 M, 10.0 mL) $AgNO_3$ (0.4267 g), $Eu(CH_3CO_2)_3{\cdot}xH_2O$ (0.8242 g), and $SrCl_2{\cdot}6H_2O$ (0.6692 g), respectively, as well as a solution of Na_2CO_3 (1.00 M, 20.0 mL) (2.1208 g). $AgNO_3$, $Eu(CH_3CO_2)_3{\cdot}xH_2O$, and $Cl_2Sr{\cdot}6H_2O$ solutions were then combined in a 1 : 1 : 1 ratio in a beaker and rapidly agitated for five minutes at room temperature. The next step involved gradually adding the 1.00 M Na_2CO_3 solution to the mixture above while stirring to ensure that all of the metal salts' carbonates had precipitated. The finished mixture was continuously swirled for four hours at 55 to 60 °C. Then, the precipitation of white metal carbonate was filtered and repeatedly washed with DW. Following filtration, the precipitate was dried in an oven set at 120 °C for two hours. The resulting dry precipitate was calcined for five hours at 600 °C in a muffle furnace to make NMs. A NM was created as a result of the calcination procedure (Scheme 1). Strontium carbonate did not break down into its oxide because strontium oxide requires a temperature greater than 900 °C to produce oxide.[51] The reaction of the NMs is as follows:

Precipitation steps:

$$(2Ag^+ + 2NO_3^-) + (2Na^+ + CO_3^{2-}) \rightarrow Ag_2CO_3 + 2(Na^+ + NO_3^-)$$

$$2(Eu^{3+} + 3CH_3CO_2^-) + 3(2Na^+ + CO_3^{2-}) \rightarrow Eu_2(CO_3)_3 + 6(Na^+ + CH_3CO_2^-)$$

$$(Sr^{2+} + 2Cl^-) + (2Na^+ + CO_3^{2-}) \rightarrow SrCO_3 + 2(Na^+ + Cl^-)$$

Calcination steps:

$$Ag_2CO_3 \xrightarrow{\text{calcination}} 2Ag + CO_2$$

$$Eu_2(CO_3)_3 \xrightarrow{\text{calcination}} Eu_2O_3 + CO_2$$

$$SrCO_3 \xrightarrow{\text{calcination}} SrCO_3$$

$$Ag + Eu_2O_3 + SrCO_3 \rightarrow Ag{\cdot}Eu_2O_3{\cdot}SrCO_3$$

Dye removal study

CV dye was used to examine the photocatalytic activity of $Ag{\cdot}Eu_2O_3{\cdot}SrCO_3$ NMs in ambient conditions. Different volumes of catalyst were put into a cylindrical Pyrex beaker with a diameter of 5 cm, which contained the dye solution (100 mL, initial concentration 5.0 ppm). Before the irradiation, the solution was stirred for approximately an hour in the dark to ensure adsorption/desorption equilibrium. Two 200 W, 220–240 volt tungsten filament light bulbs were used as a visible light source. The experimental dye solution and the light source were separated by 25 cm. Before analysis, dye solutions were centrifuged to extract them from the photocatalyst after 4 mL of the solutions were periodically collected. A Shimadzu-1800 double-beam UV-vis spectrophotometer was used to quantify the change in dye solution concentration spectrophotometrically. A range of catalyst doses was examined. The following formula was used to determine the catalytic efficiency of dye degradation:

$$\text{Efficiency } (\%) = \frac{(C_0 - C_t)}{C_0} \times 100 = \frac{(A_0 - A_t)}{A_0} \times 100 \quad (1)$$

where C_t and A_t stand for the concentration and absorbance of the dye solution after irradiation, and C_0 and A_0 for the concentration and absorbance of the dye solution before irradiation, respectively.

Also, the first-order reaction kinetics can be represented by the following eqn (2)

$$\ln(A_t) = \ln(A_0) - kt \quad (2)$$

where k (min^{-1}) is the reaction rate constant, which can be calculated from the slope $-\ln(A_t)$ *vs.* time (t). We can also calculate the required time for degrading half ($t_{1/2}$, half-life) from its initial value by using the following eqn (3)–(6)

$$(A_t)_{1/2} = (A_0)/2 \quad (3)$$

$$\ln\left(\frac{A_t}{A_0}\right) = -kt \quad (4)$$

$$\ln 2 = kt_{1/2} = 0.693 \quad (5)$$

$$t_{1/2} = \frac{0.693}{k} \quad (6)$$

Using CV dye at various NM concentrations and pH values, the adsorption capacity of the NMs was assessed. The sample solution was centrifuged following an hour of stirring in the dark to achieve adsorption–desorption equilibrium. The initial and equilibrium concentrations of CV dye were measured using a UV-vis spectrophotometer. Using eqn (7), the adsorbent's ability to absorb dye in the dark was determined.

$$\text{Adsorption } (\%) = \frac{(C_i - C_{eq})}{C_i} \times 100 = \frac{(A_i - A_{eq})}{A_i} \times 100 \quad (7)$$

here, C_i and A_i stand for the concentration and absorbance of the initial dye solution, and C_{eq} and A_{eq} stand for the concentration and absorbance of the dye solution after being adsorbed by the catalyst in the absence of light (equilibrium point), respectively.

The adsorption capacity of the NMs was calculated using the following eqn (8)

$$\text{Adsorption capacity } (Q_e) = \frac{(C_0 - C_{eq})}{mV} \quad (8)$$

where Q_e (mg g^{-1}) is the adsorption capacity at equilibrium, C_0 (mg L^{-1}) and C_{eq} (mg L^{-1}) are the initial and equilibrium point concentrations of CV dye, respectively, V (L) is the volume of CV dye solution, and m (g) is the amount of adsorbent (catalyst).

Detection of the hydroxyl radical

During photocatalysis, the hydroxyl radical ($^{\bullet}OH$) was detected using sodium hydroxide (NaOH) and terephthalic acid (TA) in the $Ag{\cdot}Eu_2O_3{\cdot}SrCO_3$ NMs. Initially, 100 mL of DW and 8.6 mg of TA were taken and added to a beaker. After that, NaOH was added until all of the TA had interacted with it. For the sodium terephthalate salt to adequately develop, the solution was

agitated for one to two hours.[52] To measure the amount of •OH produced by the Ag·Eu_2O_3·$SrCO_3$ NMs, TA was employed as a probe molecule. Three pH conditions (acidic, neutral, and basic) were used to measure the generation of •OH radicals in the synthesized NMs. Initially, a predetermined amount of NM was combined with the freshly made sodium terephthalate salt solution. The mixture was stirred in a dark chamber for one hour. The solution was then exposed to visible light using two 200 W, 220–240 volt tungsten filament light bulbs. Sodium terephthalate and •OH combine easily to form sodium 2-hydroxyterephthalate, a highly luminous chemical. A Shimadzu Crop. The Model RF-5301 spectrofluorophotometer was used to measure the amount of sodium 2-hydroxyterephthalate generated following centrifugation. When stimulated at a wavelength of 315 nm, this acid exhibits a fluorescence peak at around 425 nm, facilitating the detection of •OH by the fluorescent technique.[53]

Fabrication of a GCE with Ag·Eu_2O_3·$SrCO_3$ NMs

The working electrode, which is an important element of the proposed sensor, was manufactured by GCE with Ag·Eu_2O_3·$SrCO_3$ NMs. In this process, a thin coat of Ag·Eu_2O_3·$SrCO_3$ NM slurry was prepared with ethanol and applied on the already cleaned GCE surface using the drop-cast method, followed by drying under ambient laboratory conditions. To increase stability and prolong the life of the electrode, a 5 μL amount of 5% Nafion solution was added to the NM layer using the drop-cast method. The electrode was then left to dry at room temperature. An Autolab Potentiostat, Metrohm, in three-electrode mode, was used to carry out electrochemical measurements. Here, the GCE was the working electrode, the reference electrode was an Ag/AgCl (Saturated KCl) electrode, and the counter electrode was a platinum (Pt) electrode.

Results and discussion

Structural characterization of Ag·Eu_2O_3·$SrCO_3$ NMs

XRD of Ag·Eu_2O_3·$SrCO_3$ NMs was performed for structural characterization and to determine the composition and phases of the NMs, as shown in Fig. 1. The XRD data analysis of NMs was carried out using MDI Jade software. The synthesized NMs have matching peaks at 2θ angles of 38.11° (1 1 1), 44.31° (2 0 0), 64.44° (2 2 0), and 77.41° (3 1 1). The peak search results matched the obtained pattern for the structure of silver 3C NPs, Ag (matching PDF#87-0597, intensity matching 85%), indicating a cubic shape. It showed the space group of the Ag, $Fm\bar{3}m$ (225), cell dimension (a) 4.0862 Å, and angle (α) 90°. The unit cell volume of Ag is 68.2 $Å^3$. The presence of Eu_2O_3 was predicted by the matching peaks at 2θ values of 28.43° (2 2 2), 32.94° (4 0 0), 38.84° (3 3 2), 40.64° (4 2 2), 42.38° (1 3 4), 45.68° (5 2 1), 47.27° (4 4 0), 48.82° (4 3 3), 51.81° (2 3 5), 53.26° (0 2 6), 54.69° (1 4 5), 56.08° (6 2 2), 57.46° (1 3 6), 58.82° (4 4 4), 60.15° (5 4 3), 62.77° (6 3 3), 64.06° (6 4 2), and 67.84° (1 5 6) (matching PDF#43-1008, intensity matching 37%), which is cubic in shape. The space group of Eu_2O_3 is $Ia\bar{3}$ (206) with cell dimensions: (a) 10.8683 Å and angle (α) 90° and a unit cell volume of 1283.8 $Å^3$. Finally, the matching peaks of $SrCO_3$ at 2θ value of 25.19° (1 1 1), 25.84° (0 2 1), 35.14° (2 0 0), 36.57° (1 3 0), 41.36° (2 2 0), 44.13° (0 3 2), 45.71° (0 4 1), 47.76° (1 3 2), 49.97° (1 1 3), 51.71° (2 2 2), 53.65° (1 2 3), 56.32° (1 4 2), 57.28° (3 1 1), 58.93° (2 4 1), 59.9° (1 5 1), 62.64° (0 1 4), 72.07° (3 3 2), and 77.38° (1 6 2) (matching PDF#84-1778, intensity matching 38%). The shape of $SrCO_3$ is orthorhombic, with the *Pmcn* (62) space group; with cell dimensions (a) 5.1039 Å, (b) 8.4022 Å, (c) 6.022 Å, and angle (α) 90°, and the unit cell volume 258.3 $Å^3$. Scherrer's formula was used to analyze the average particle size from the XRD data. The equation was:

$$\tau_{avg} = k\lambda/\beta \cos\theta \quad (9)$$

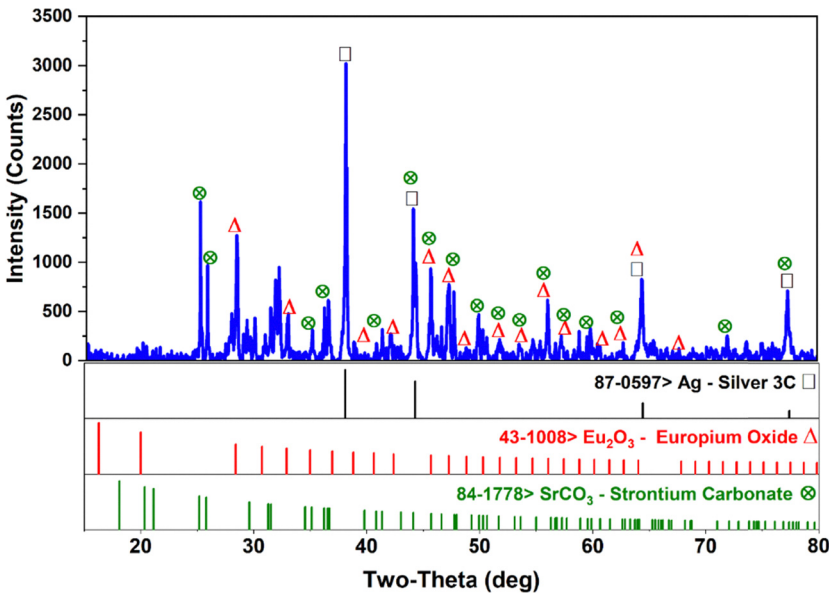

Fig. 1 XRD pattern of Ag·Eu_2O_3·$SrCO_3$ NMs.

where λ is the X-ray wavelength (0.1506 nm), β is the line broadening at half the maximum intensity (FWHM), θ is the Bragg angle, and τ is the mean size. k is a dimensionless form factor with a value of 0.94. The average particle size was 53.62 nm. The dislocation density (η) and lattice strain (ε) were also calculated using the following equations,[54,55] and the values were 3.5×10^{-4} nm^{-2} and 9.4×10^{-4}, respectively. The good crystallinity of the Ag·Eu_2O_3·$SrCO_3$ NMs is confirmed by the small values of η and ε obtained in this study.

$$\eta = 1/\tau_{avg}{}^2 \quad (10)$$

$$\varepsilon = \beta \cos\theta/4 \quad (11)$$

The reference intensity ratio (RIR) approach was used to determine the phase % of NMs. The following equation was utilized to carry out the quantitative analysis of XRD patterns using MDI Jade 6.5:

$$W_i = \frac{\frac{I_i}{\mathrm{RIR}_i}}{\sum_{j=1}^{n} \frac{I_j}{\mathrm{RIR}_j}} \times 100 \quad (12)$$

where W_i is the weight fraction (weight percent, wt%) of phase I, I_i is the integrated intensity (area) of one of the primary peaks of phase I, and RIR_i is the associated RIR value.[56] Table S1 includes information on the components' I_i and RIR_i values. Ag, Eu_2O_3, and $SrCO_3$ weight percentages in Ag·Eu_2O_3·$SrCO_3$ NMs were determined to be 30.35, 27.96, and 41.69%, respectively.

Surface analysis of Ag·Eu_2O_3·$SrCO_3$ NMs

The morphology of Ag·Eu_2O_3·$SrCO_3$ NMs was revealed by the SEM images at different magnifications (Fig. 2). The Ag·Eu_2O_3·$SrCO_3$ NMs in the matrix exhibit flake-like and spherical formations with varying size distributions. The small spheres are attached to the surface of flakes (Fig. 2d).

EDS analysis of Ag·Eu_2O_3·$SrCO_3$ NMs

The EDS spectrum of Ag·Eu_2O_3·$SrCO_3$ NMs is shown in Fig. 3. The presence of four atoms (Ag, Eu, Sr, and O) was confirmed by the EDS spectrum. Additionally, the EDS mapping showed that the elements were dispersed across the matrix (Fig. S1).

FTIR spectroscopy of Ag·Eu_2O_3·$SrCO_3$ NMs

The FTIR spectrum of the Ag·Eu_2O_3·$SrCO_3$ NMs is shown in Fig. 4. The low-frequency bands of the M–O and O–M–O vibration modes (where M = Ag, Eu, and Sr) are found in the 400–1100 cm^{-1} region. The band of Ag–O vibration was observed at 432.05 cm^{-1}. Two peaks for Eu–O were detected;

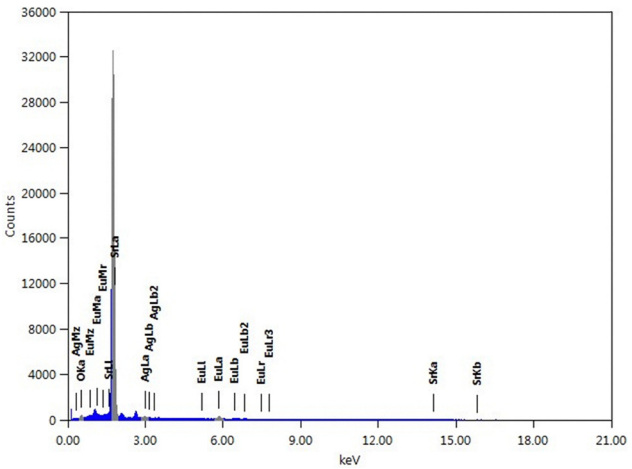

Fig. 3 EDS spectrum of Ag·Eu_2O_3·$SrCO_3$ NMs.

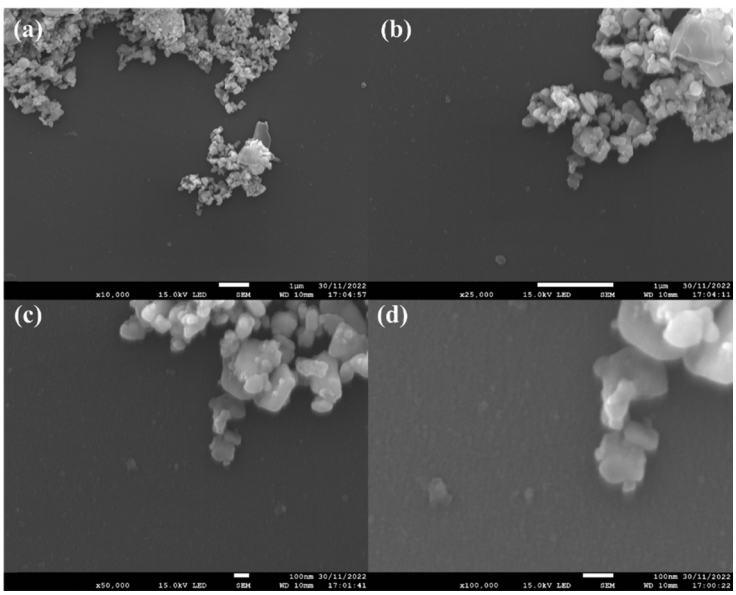

Fig. 2 SEM images of Ag·Eu_2O_3·$SrCO_3$ NMs at different magnifications (a)–(d).

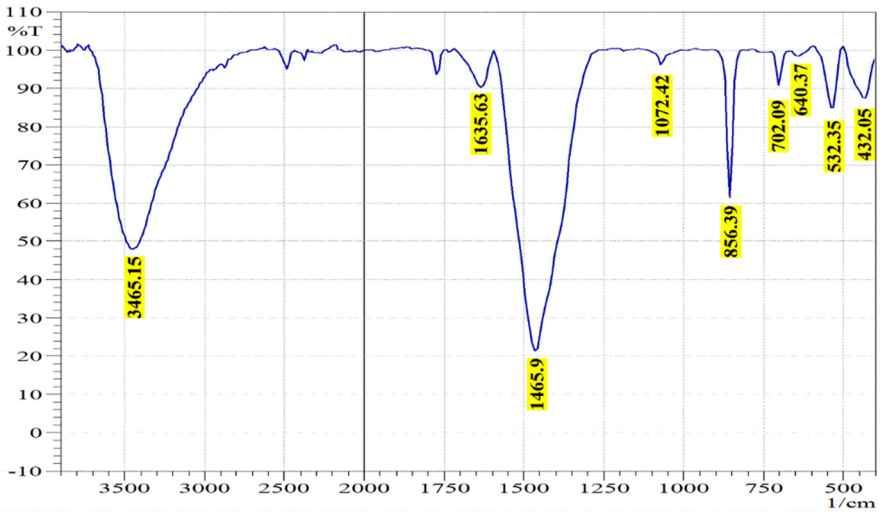

Fig. 4 FTIR spectrum of Ag·Eu_2O_3·$SrCO_3$ NMs.

their respective frequencies were 532.35 and 640.37 cm^{-1}. Eu–O bending was ascribed to 532.35 cm^{-1}, indicating the generation of Eu_2O_3.[57] $SrCO_3$ (CO_3^{2-} has D_{3h} symmetry) exhibits absorption bands at 400–1800 cm^{-1} for CO_3^{2-}. The strong absorption bands for CO_3^{2-} have centers at approximately 1072.46 and 1465.9 cm^{-1}, designated as the ν_2 mode and the asymmetric stretching vibration, respectively. Strong, narrow absorption bands for $SrCO_3$ are attributed to in-plane and out-of-plane bending vibrations, respectively, at 856.39 and 702.09 cm^{-1}, as reported in a previous study.[58,59] The hydroxyl group, O–H stretching mode, is what causes the broad absorption band at 3465.15 cm^{-1}. The water H–O–H bending vibration may be the cause of the band at 1635.63 cm^{-1}.[60] Therefore, Ag–O (432.05 cm^{-1}), Eu–O (532.35 and 640.37 cm^{-1}), and $SrCO_3$ (856.39 and 702.09 cm^{-1}) all displayed different characteristic peaks of the Ag·Eu_2O_3·$SrCO_3$ FTIR spectra.

Photoluminescence properties of Ag·Eu_2O_3·$SrCO_3$ NMs

The PL excitation and emission spectra of Ag·Eu_2O_3·$SrCO_3$ NMs are shown in Fig. 5 and Table S2. At different monitored wavelengths, the synthesized NMs showed PL excitation. A single peak was observed at 386 nm for the 450 nm monitor and at 390 nm for the 500 nm monitor. Additionally, two excitation peaks were found at 386 and 465 nm, and 388 and 468 nm, respectively, at the monitored wavelengths of 550 and 600 nm (Fig. 5(a)).

Different PL emission spectra were observed when the Ag·Eu_2O_3·$SrCO_3$ NMs were excited at different wavelengths (Fig. 5(b)). Two emission peaks were noted at 386 and 471 nm wavelengths for both 220 and 250 nm excitation. Near band edge (NBE) at 386 nm may be arising from Ag NPs, and emission at 471 nm due to $^5D_0 \rightarrow {}^7F_0$ transitions of the Eu^{3+} ions. At 300 nm excitation, 2 peaks were exhibited (403 and 462 nm). The higher energy 403 nm peak may be from Ag NPs, and the 462 nm peak may be from Ag^0 or $^5D_0 \rightarrow {}^7F_0$ transitions of Eu^{3+} ions or both. At 350 nm excitation, 3 peaks were observed at 399, 426, and 460 nm. Among them, the 399 nm peak may be assigned to the Eu–O 4f → 4f transitions, and the 426 and 460 nm bands may originate from $^5D_0 \rightarrow {}^7F_0$ transitions of Eu^{3+} or from ionized oxygen vacancies or both.[61] The 426 nm blue PL peak may also arise from $SrCO_3$. For 400 and 450 nm excitation, the emission peaks were observed at 473 and 509 nm, respectively. At 509 nm, the green PL emission observed was from Eu^{3+} ions, specifically corresponding to the $^5D_1 \rightarrow {}^7F_1$ transitions. The emission peak observed at 473 nm may be assigned to the $^5D_0 \rightarrow {}^7F_0$ transitions of Eu^{3+} in Ag·

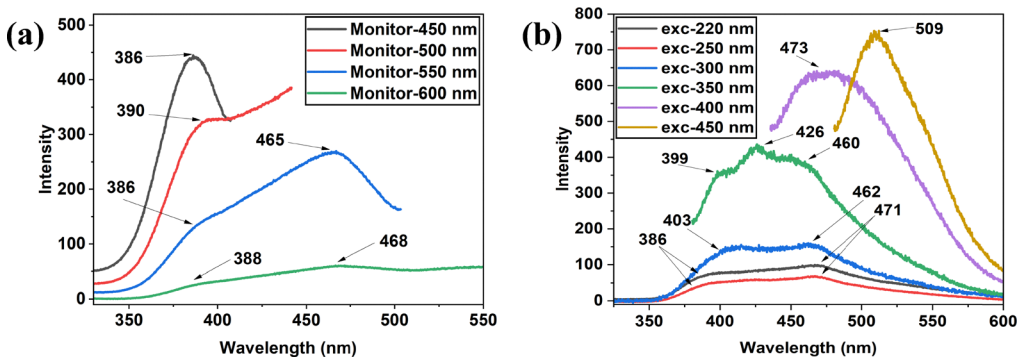

Fig. 5 PL (a) excitation spectra when monitored at various wavelengths and (b) emission spectra at various wavelengths of excitation of Ag·Eu_2O_3·$SrCO_3$ NMs.

Eu_2O_3·$SrCO_3$. The characteristic emission peak of Eu^{3+} in Eu_2O_3 is frequently observed in the 610–615 nm range, for the $^5D_0 \rightarrow {}^7F_2$ transitions, which is absent in Ag·Eu_2O_3·$SrCO_3$.[62] Herein, the 610–615 nm peak is absent due to PL quenching by the nearby metal oxides through excited-state energy transfer. $SrCO_3$ exhibited a wide range of PL emissions in the UV to visible regions. The UV region emission, also known as NBE, would be recognized for defects such as intrinsic electronic transitions, and the visible region, also known as deep-level emission (DPE), is due to localized defects in the crystal structure that produce new energy levels in the band gap, like interstitials or oxygen vacancies.[23] In the visible spectrum, the emission band between 420 and 470 nm denotes a blue band. The valence band's ionized oxygen vacancies could be the cause of the blue-band emission. The photogenerated holes may have undergone radiative recombination with electrons occupying the oxygen vacancies, leading to the detection of a blue emission. Ag·Eu_2O_3·$SrCO_3$ exhibits excitation-wavelength-dependent photoluminescence features, which can be attributed to the ground-state molecular distribution differing in energy and a low rate of excited-state relaxation processes, indicating a violation of Kasha's rule.[63] "Anti-Kasha" behavior occurs when higher excited states emit directly or relax slowly. Finally, emissions observed from Ag, $SrCO_3$, and Eu_2O_3 are either in overlapping or matching energy levels, indicating high possibilities of energy transfer, and different color emissions observed are suitable for multicolor phosphor materials. Excitation wavelength-dependent flexible electronic and PL behavior could be suitable for transistor or display applications, revealing promising PL properties of Ag·Eu_2O_3·$SrCO_3$.

Raman spectrum of Ag·Eu_2O_3·$SrCO_3$ NMs

The Raman spectrum of Ag·Eu_2O_3·$SrCO_3$ is shown in Fig. 6. The Raman bands for Eu–O are located at 102 and 246 cm^{-1}, and exhibit F_g and $E_g + F_g$ symmetry, respectively, for C-type (cubic) Eu_2O_3.[61] Peaks for $SrCO_3$ were found at 147 and 1073 cm^{-1}. Raman lines at 147 cm^{-1} control the spectra and are ascribed to angular oscillations of A_{1g} modes. The symmetric stretching mode (ν_1-CO_3^{2-}) of the carbonate group (CO_3^{2-}) is responsible for the peak at 1073 cm^{-1}.[64] The OH stretching vibration was measured at 3298 cm^{-1}.[65]

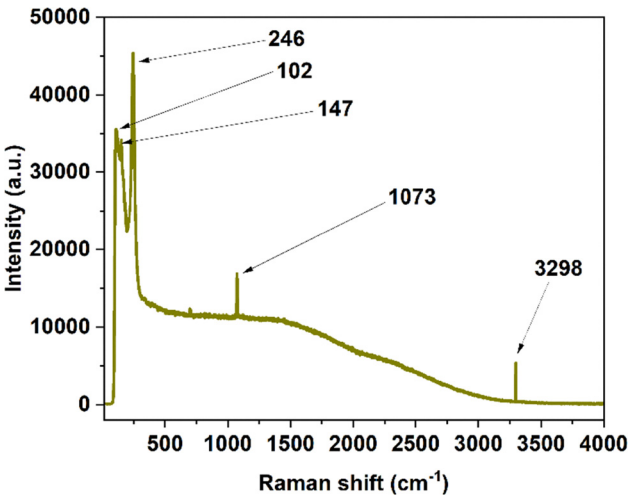

Fig. 6 Raman spectrum of Ag·Eu_2O_3·$SrCO_3$ NMs.

Evaluation of photocatalytic activity

The effective dose of Ag·Eu_2O_3·$SrCO_3$ NMs for dye removal when subjected to visible light irradiation was ascertained using a variety of doses, as shown in Fig. 7(a) and Fig. S2. To develop different solutions for this experiment, photocatalyst doses ranging from 0.05 g to 0.07 g were used. For 0.05 g, 0.06 g, and 0.07 g, respectively, the observed greatest percentage of CV elimination was 0.06 g with 97.46%, 97.7%, and 97.45%. As the amount of photocatalyst was increased, the percentage of CV elimination increased continuously. However, efficiency began to fall after reaching its highest peak for the advised dosage of 0.06 g.

Fig. 7(b)–(d)demonstrate the gradual dye elimination in the presence of the Ag·Eu_2O_3·$SrCO_3$ photocatalyst at pH 9.2, 7, and 4. The elimination efficiencies were determined to be 97.7%, 97.48%, and 3.14% at pH 9.2, 7, and 4, respectively, after 150 minutes of visible light irradiation. The percentage of dye removal yield was determined to be outstanding in basic medium (pH 9.2), moderate in neutral medium (pH 7), and poor in acidic medium (pH 4), due to the generation of hydroxyl radicals at pH 9.2. The photocatalytic effectiveness of different catalysts in the degradation of CV dye is compared to a synthesized NM, Ag·Eu_2O_3·$SrCO_3$, in Table 1. Each entry in the table includes details about the photocatalyst, dye concentration, irradiation source, catalyst dose, degradation time, efficiency, and matching reference.

For different pH values, the plot of (−ln[CV]) *vs.* time displays a straight line with slope k (Fig. 7(e)). The experimental results were well described by the first-order assumption. Table S3 lists the calculated dye degradation rate constants (k) and r-squared (r^2) values. The corresponding r^2 values for pH 4, pH 7, and pH 9.2 were 0.8444, 0.772, and 0.9648. The half-life of the dye degradation at different pH levels could be calculated by using eqn (6). For pH 4, 7, and 9.2, the $t_{1/2}$ values were 101.911, 29.615, and 25.955 min, respectively. This showed that, in contrast to acidic medium, basic medium and neutral medium produced more ROS, which accelerated the elimination of half of the dye concentration.

Recycling assays were used to determine the stability of the Ag·Eu_2O_3·$SrCO_3$ catalyst at pH 9.2; the results are displayed in Fig. 7(f)–(m). Reclamation and reuse are crucial to the photocatalytic process because they reduce the system's cost for wastewater treatment and other processes. An uncomplicated procedure was used to replenish the photocatalyst. The solution was allowed to stand for 24 hours after the initial photocatalytic dye degradation reaction was finished, and then the supernatant was separated. The catalyst was then thoroughly rinsed several times with DW and acetone. After that, the catalyst was dried at 120 °C for two hours. To evaluate the photocatalytic efficacy of the recycled catalyst, a series of tests was carried out employing 0.06 g of catalyst under visible light

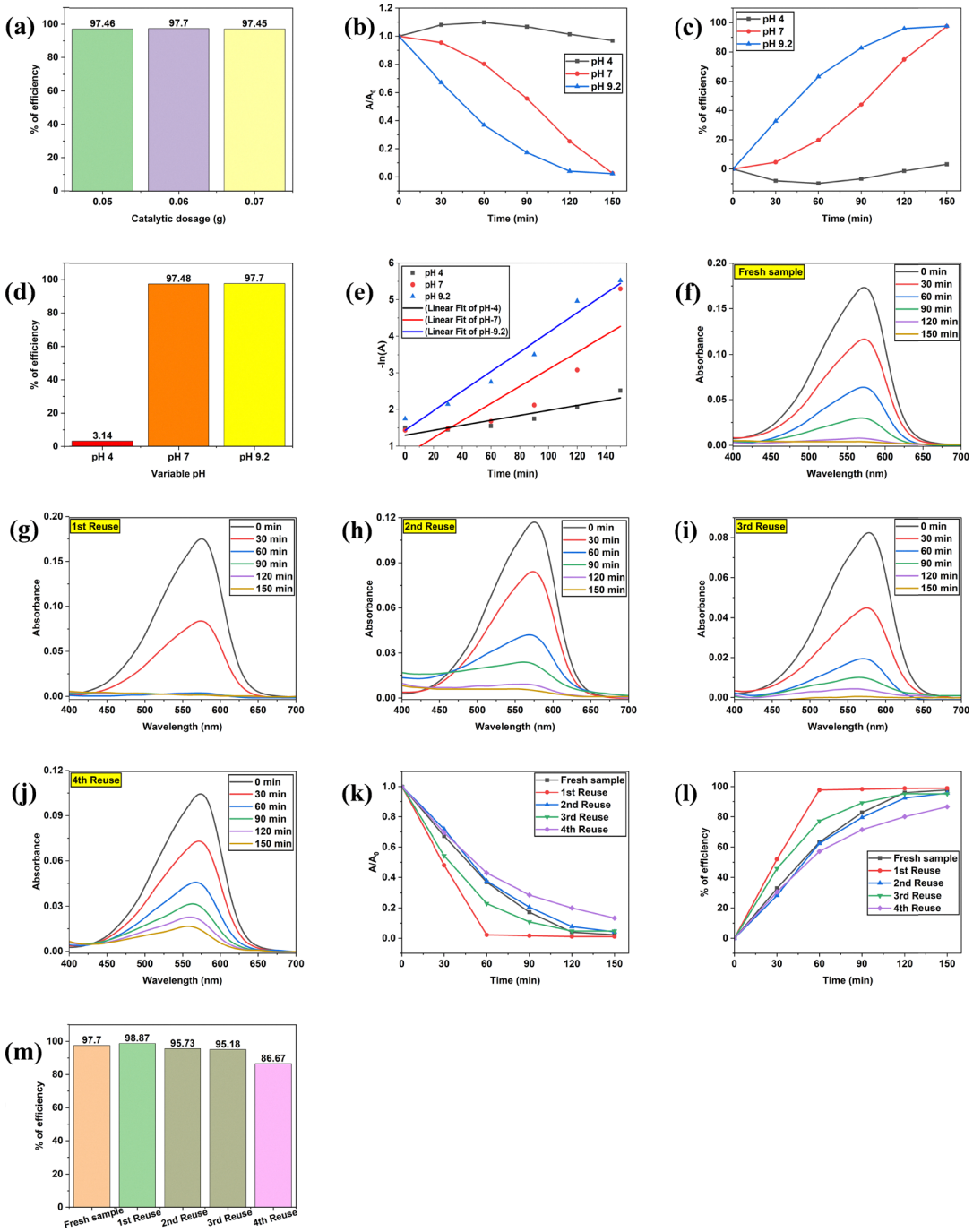

Fig. 7 Photocatalytic activity of Ag·Eu_2O_3·$SrCO_3$ NMs using CV dye (5 ppm) under visible light irradiation for 150 minutes, (a) dose effect, (b)–(d) pH effect, (e) kinetics study, and (f)–(m) catalytic stability.

at pH 9.2 using CV dye solution. The catalyst was used once more for the degradation of a fresh CV solution under the same conditions for each new cycle following the separation and drying of the photocatalyst samples (Fig. 6(f)–(j)). The dye degradation over time in each cycle is depicted in Fig. 6(k). The percentage of CV dye degradation efficiency for each cycle is displayed in Fig. 6(l) and (m). In the presence of the Ag·Eu_2O_3·$SrCO_3$ catalyst at pH 9.2, the degradation percentages of the CV solution for five cycles of use were 97.7%, 98.87%, 95.73%, 95.18%, and 86.67%, respectively, following 2.5 hours of exposure to visible light. However, 86.67% of the CV was successfully degraded after the fourth photocatalyst reuse, resulting in a total efficiency loss of 11.03% during the five cycles. This implies that dye can be successfully removed by the catalyst.

Effect of the amount of adsorbent and pH on the removal of CV dye in the dark

For determining the adsorption efficiency of the synthesized NMs, CV dye was used. Fig. 8(a) represents the absorbance of CV dye initially, and with different amounts of adsorbent (at the

Table 1 A comparison between the Ag·Eu_2O_3·$SrCO_3$ NM photocatalyst and other CV dye removal photocatalysts

Catalyst	Dye conc. (ppm)	Irradiation source	Catalyst dose	Time (min)	Efficiency (%)	Ref.
Ag·Eu_2O_3·$SrCO_3$ NMs	5	Tungsten filament (200 W)	0.6 g L^{-1}	150	97.7	This work
C-MIL-53(Fe)@BiOI heterojunction	10	LED (5 W)	0.55 g L^{-1}	38	96.8	66
Sr–ZnO/AC nanoneedles	20	UV	100 mg	120	98.92	67
MWC/ZnO composite	—	Visible	—	180	94.4	68
TiO_2@C composite	20	UV	0.025 g	300	98.1	69
		Visible			95.9	
IONPs	10	Sunlight	1 mg mL^{-1}	210	99.23	70
MgO NPs	10	UV	0.2 g	130	99.19	71
MgO–Ben nanocomposite			0.15 g		83.38	
$NiFe_2O_4$ NPs	10	Mercury lamp (6 W)	0.05 g L^{-1}	120	75.5	72
MoS_2–NiO–CuO nanohybrid	20	Halogen (500 W)	0.02 g	80	94	73

equilibrium point, pH 9.2). Here it was observed that the absorbance of CV dye decreases with increasing the amount of adsorbent. In Fig. 8(b) and Table S4, the adsorption percentage and capacity were displayed. For 0.05 g of adsorbent, the adsorption percentage and capacity were 1.99% and 34.8 mg g^{-1}, respectively. And for 0.06 g and 0.07 g, the adsorption percentages were 13.433% and 21.891%, respectively. Also, the adsorption capacity increased to 112 mg g^{-1} and 156.429 mg g^{-1}, respectively. More active binding sites and a larger sorption surface area are the reasons for the rising percentage of adsorption and adsorption capacity with increased adsorbent dose.[74]

In Fig. 8(c), the CV dye absorbance was compared with different pH levels (4, 7, and 9.2) with the same adsorbent (0.06 g). Here, it is observed that at the equilibrium point, the absorbance of CV dye was increased in acidic (pH 4) and neutral (pH 7) medium. For this reason, the adsorption percentage and capacity exhibited a negative value (Fig. 8(d) and Table S4). But for basic medium (pH 9.2), the absorbance, adsorption percentage, and capacity showed positive results. The reason behind this is that the electrostatic interaction with the ions' adsorption surface in the reaction mixture often determines the impact of a solution's pH. Both the chemistry of the solution and the adsorbents' surface binding sites can be impacted by the pH of the solution.[75] In the basic media, the cationic dye CV performs better. Because the cationic charges in the dye ensure that they are drawn to the adsorbent's negative surface charge, the adsorption capacity and removal

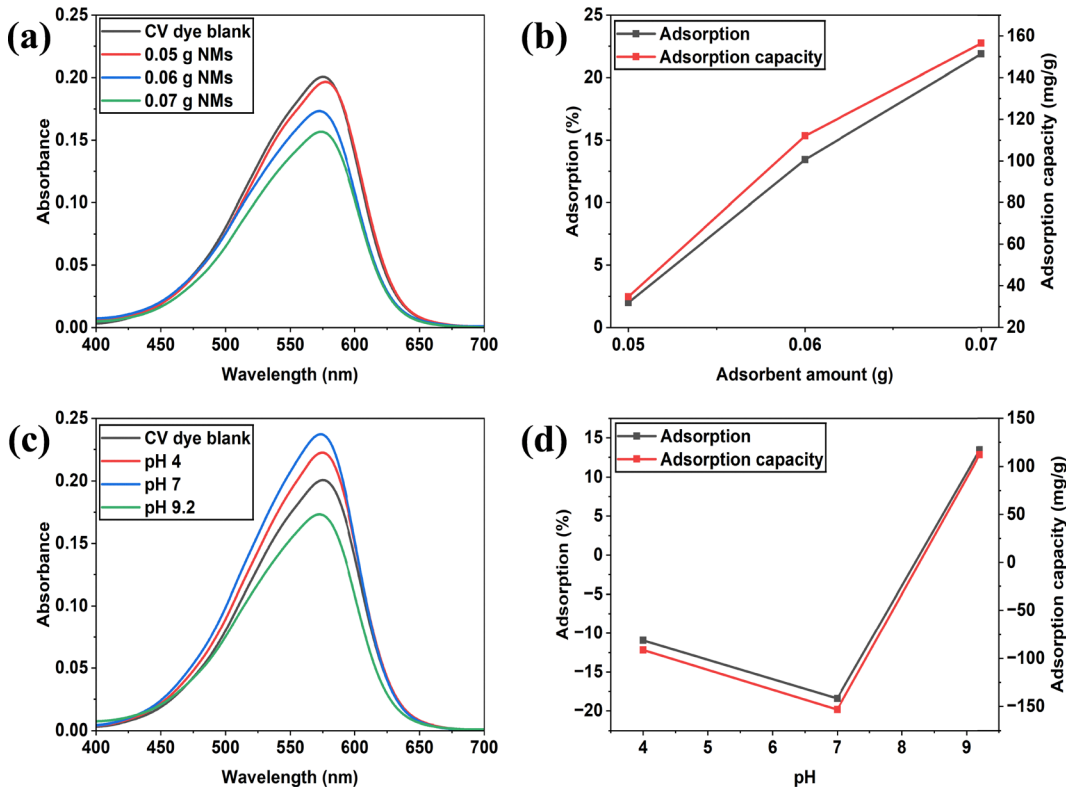

Fig. 8 CV dye absorbance, adsorption percentage and adsorption capacity in the dark at (a) and (b) different doses of Ag·Eu_2O_3·$SrCO_3$ NMs (0.05 g, 0.06 g and 0.07 g) and (c) and (d) different pH (4, 7, 9.2) with a 0.06 g amount of the NMs.

of basic dyes increased when the pH of the solution was high. As a result, the adsorbents and sorbates in the solution are certainly attracted to each other electrostatically.[76] The adsorbent and the CV dye repel each other electrostatically at lower pH because the surface is more positively charged. Conversely, increasing pH causes the adsorbent's surface to become negatively charged, which increases the electrostatic attraction between the surface and the positively charged CV dye molecules and increases adsorption.[77]

Hydroxyl radical (•OH) generation during photocatalysis of Ag·Eu_2O_3·$SrCO_3$ NMs at different pH values under visible light

The generation of •OH radicals during photocatalysis of Ag·Eu_2O_3·$SrCO_3$ NMs at different pH levels was detected by using sodium terephthalate solution (Fig. 9). Here, we observed that radical generation of synthesized NMs was higher at basic medium (pH 9.2) rather than neutral (pH 7) and acidic medium (pH 4). The result indicated that the synthesized NMs would be a good catalyst for dye removal in a basic medium, which also supports and matches the photocatalytic CV dye removal data under different conditions (Fig. 7(b)–(d)).

Mechanism of CV dye degradation using Ag·Eu_2O_3·$SrCO_3$ photocatalysts

Driven by visible light and ROS, the photocatalytic activity of Ag·Eu_2O_3·$SrCO_3$ NMs showed outstanding performance through the destruction of the CV dye. Ag·Eu_2O_3·$SrCO_3$ is a reusable and stable photocatalyst that could be used to remediate industrial wastewater.

From previous works, we found that Ag NP size has a major impact on localized surface plasmon resonance (SPR) and electron–hole separation efficiency. Additionally, the SPR of Ag is crucial for harvesting visible-light and triggering the adequate release of photoinduced electrons rather than recombination with photogenerated holes, which should contribute to the production of ROS.[15,78] Shawky *et al.* reported that, for the Ag@CuO/TiO_2 nanocomposite, the SPR of Ag NPs enhances visible-light harvesting and increases photocatalytic activity, while the difference in CB levels between CuO and TiO_2 makes it easier to separate photogenerated electrons and holes.[79] The electrostatic interaction between the carbonate created by the hydrolysis of $SrCO_3$ and the cationic chromogenic groups of CV dye (N^+) is the primary adsorption mechanism of n-type semiconductor $SrCO_3$.[25] The high affinity of $SrCO_3$ or $SrCO_3$-based composites for CV dyes (cationic dye) is mostly due to the electrostatic attraction. The surface of $SrCO_3$ develops a negative charge in an aqueous system due to the CO_3^-, which attracts the positively charged chromogenic groups of CV dye. Moreover, the photocatalyst's Eu^{3+} content most likely introduces sublevels below the conduction band, thereby improving its visible-light sensitivity.[11,80] Mohamed and Abu–Dief reported that Eu_2O_3 NPs act as an "energy reservoir" in Eu_2O_3–ZnO mixed oxide NPs, first absorbing energy and then

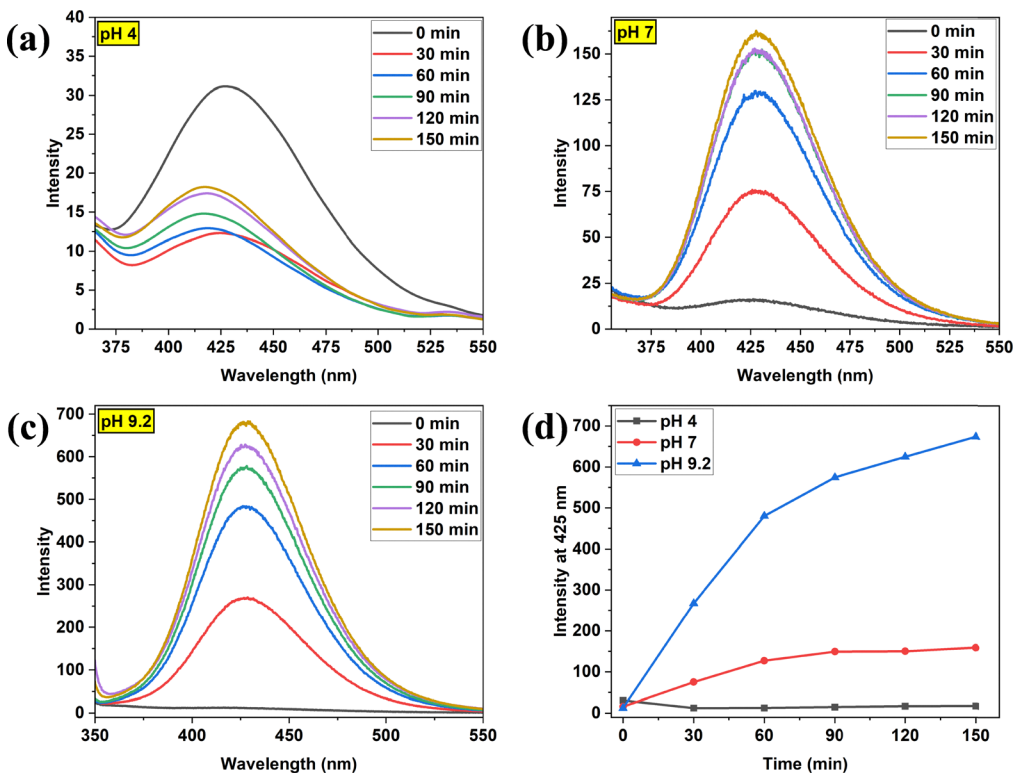

Fig. 9 Hydroxyl radical (•OH) generation during photocatalysis of Ag·Eu_2O_3·$SrCO_3$ NMs at different pH (a) pH 4, (b) pH 7, (c) pH 9.2, and (d) time-dependent intensity observation at 425 nm (under visible light).

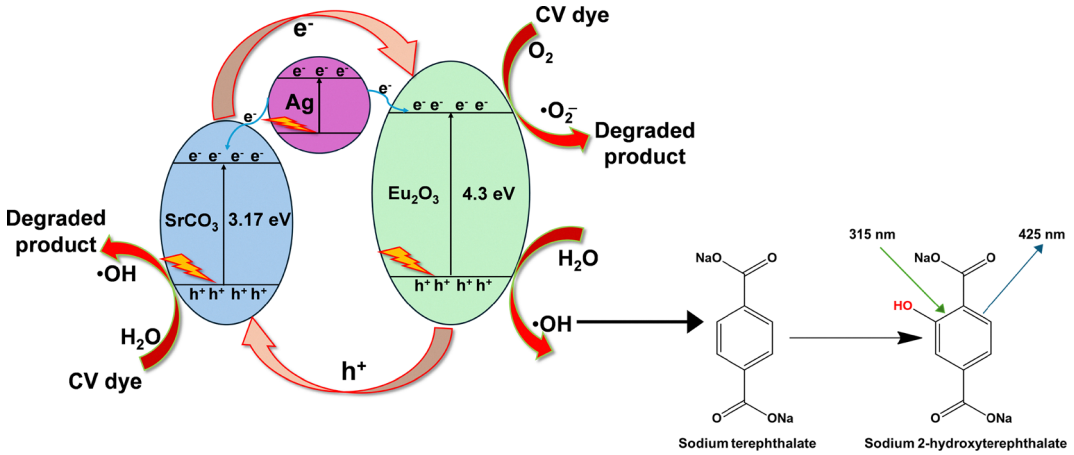

Fig. 10 An illustration of photocatalytic degradation of CV dyes by the Ag·Eu_2O_3·$SrCO_3$ NMs.

transferring it to ZnO. Under UV irradiation, electron excitations between the lanthanide electronic structure of $4f_x5d_y$ are encouraged by the proximity of the ground and excited energy states of Eu^{3+} ions in Eu_2O_3.[21] In the present study, photoexcitation generated electrons and energy that are transferred from $SrCO_3$ to Eu_2O_3, which harvests electrons and energy for transferring to nearby dissolved O_2 molecules to produce $^{\bullet}O_2^-$ radicals, and holes generated in the VB react with H_2O to form $^{\bullet}$OH radicals. Finally, these ROS degrade dye molecules to enhance photocatalysis.

A potential mechanism for the increased photocatalytic performance of the Ag·Eu_2O_3·$SrCO_3$ photocatalyst upon visible light irradiation is suggested and schematically represented in Fig. 10 based on the experimental results and review of previous literature. This mechanism demonstrates how NMs degrade CV dye by producing ROS. When Ag·Eu_2O_3·$SrCO_3$ NMs are exposed to visible light with a photon energy greater than or equal to the Ag, Eu_2O_3, and $SrCO_3$ band gaps, the electrons in the valence bands (VB) may be stimulated to the conduction bands (CB). Here, Eu_2O_3 is a p-type and $SrCO_3$ is an n-type semiconductor, whose band gaps are 4.3 and 3.17 eV, respectively.[17,23] In n-type semiconductors (where the majority of charge transporters are electrons), the energy distortion, also referred to as the Schottky Barrier (SB) height, manifests as a potential energy barrier that results in fixing behavior between the metal and the n-type semiconductor for electronic transport across the metal semiconductor (MS) interface and the essential elements of electron–hole separation and charge buildup at the surface of p-type semiconductors (where the majority of charge transporters are holes) are the SB and charge spatial distribution.[81–83] During photoexcitation, the electrons in the VB of Eu_2O_3 and $SrCO_3$ would be excited and migrate to the CB. An equal number of holes would be made in the VB at the same time. The electron moved from $SrCO_3$ to Eu_2O_3 at this point (during photoexcitation, an electron is moved from a lower energy CB to a higher energy CB), and the hole moved from Eu_2O_3 to $SrCO_3$ through carrier diffusion between the $SrCO_3$ and Eu_2O_3 until the system reached an equilibrium. During light emissions, the processes of electron and hole transfer were reversed. Ag NPs served as an electron conduction bridge between $SrCO_3$ and Eu_2O_3, allowing electrons to move from $SrCO_3$ to Eu_2O_3 continuously while also preventing electron–hole recombination.[84] As evidenced by XRD data, the Eu_2O_3 primary peak (2θ, 29) shifted to 28.43 and secondary peaks (2θ, 33, 47) shifted to 32.94 and 47.27. Furthermore, the $SrCO_3$ major peak (2θ, 25.2) slightly shifted to 25.19. This indicates the formation of Schottky contacts, Eu_2O_3–Ag–$SrCO_3$, demonstrating Ag bridging, which accelerates the photo-induced charge separation process, augments the redox capacity of semiconductor surfaces, acts as a sink for photogenerated electrons, and facilitates inhibition of electron–hole recombination and generation of ROS.[85] The PL data showed that Eu_2O_3 had a significant, most intense emission peak at 509 nm (green emission), as shown in Fig. 5. The main charge-trapping locations in the energy reservoir, Eu_2O_3, are singly ionized oxygen vacancies, which are represented by this 509 nm signal. Furthermore, the simultaneous quenching of the intrinsic emission (intrinsic NIR emission of Eu_2O_3 was not observed in Eu_2O_3–Ag–$SrCO_3$) alongside the emergence of the 509 nm peak confirms an efficient energy transfer pathway from the host lattice to the Eu_2O_3, indicating it as an energy reservoir in Eu_2O_3–Ag–$SrCO_3$ NMs.[86] During photoexcitation, the generated hole in VB reacts with H_2O and forms $^{\bullet}$OH radicals. Simultaneously, electrons in the CB reacted with absorbed O_2 and generated $^{\bullet}O_2^-$ radicals. The CV dye was degraded by these generated radicals. $^{\bullet}$OH radicals were identified by using the non-fluorescent sodium terephthalate solution. When sodium terephthalate reacted with $^{\bullet}$OH radicals, it produced sodium 2-hydroxyterephthalate, which was fluorescently active. When the solution was excited at a wavelength of 315 nm, it exhibited an emission peak at 425 nm. Reactions shown in eqn (13)–(18) demonstrate how the electron–hole pairs created on the photocatalyst provide an energy source, and react to produce ROS from the water splitting reaction ($^{\bullet}$OH, $^{\bullet}O_2^-$). These procedures are necessary for ROS in addition to a reaction with the chemisorbed CV dye for its degradation.[10]

Photoexcitation and electron–hole pair generation

$$Ag{\cdot}Eu_2O_3{\cdot}SrCO_3 + \text{Visible light } (h\nu) \rightarrow Ag{\cdot}Eu_2O_3{\cdot}SrCO_3\ (e^-_{CB} + h^+_{VB}) \quad (13)$$

$$e^- + h^+ \rightarrow \text{Energy} \quad (14)$$

Formation of $^{\bullet}OH$ radicals

$$h^+ + H_2O \rightarrow H^+ + {}^{\bullet}OH \quad (15)$$

Formation of $^{\bullet}O_2^-$ radicals

$$e^- + O_2 \rightarrow {}^{\bullet}O_2^- \quad (16)$$

CV dye degradation

$$^{\bullet}OH + \text{CV dye} \rightarrow \text{Degraded product (major)} \quad (17)$$

$$^{\bullet}O_2^- + \text{CV dye} \rightarrow \text{Degraded product (minor)} \quad (18)$$

Antibacterial activity of $Ag{\cdot}Eu_2O_3{\cdot}SrCO_3$ NMs

Several variables, such as size, shape, and crystal growth behavior, make NMs extremely hazardous to bacteria.[87] In nutrient broth media, the pathogenic bacterial isolates were precultured at 37 °C and agitated at 120 rpm for the duration of the night. 1, 2, and 3 mg mL^{-1} amounts of NMs were used to prepare the samples. To cultivate the pure cultures of the organisms, Mueller–Hinton agar nutrients were utilized. The agar medium was used to make a well that was about 6 mm in diameter and 4 mm deep. Using a micropipette, roughly 60 mL of solution was added to each well of the constructed NM solutions, with gentamicin (CN 10) serving as a control. After incubating the plates for 24 hours at 37 °C, the different degrees of zone inhibition were assessed.

Using the agar well diffusion method, the antibacterial properties of the NMs $Ag{\cdot}Eu_2O_3{\cdot}SrCO_3$ were evaluated against a number of harmful bacteria, such as *Staphylococcus aureus*, *Klebsiella pneumoniae*, *Pseudomonas aeruginosa*, and *Proteus mirabilis*. The outcomes are displayed in Fig. 11. When exposed to the produced NMs, they demonstrated comparable bacterial killing ability for both Gram-positive and Gram-negative bacteria. Gram-positive *Staphylococcus aureus* bacteria were eliminated with a 3.33 ratio using 3 mg mL^{-1} of NMs. Likewise, Gram-negative bacteria *Klebsiella pneumoniae*, *Pseudomonas aeruginosa*, and *Proteus mirabilis* were inhibited with a 3.33, 3.17, and 3.17 ratio for 3 mg mL^{-1} (Table S5). The production of ROS improved the killing of bacteria *via* the ROS mechanism. The toxicity of metal oxide is often ascribed to ROS generation. The bacterial cell walls may be significantly damaged as a result of the NMs' efficacy.[88,89]

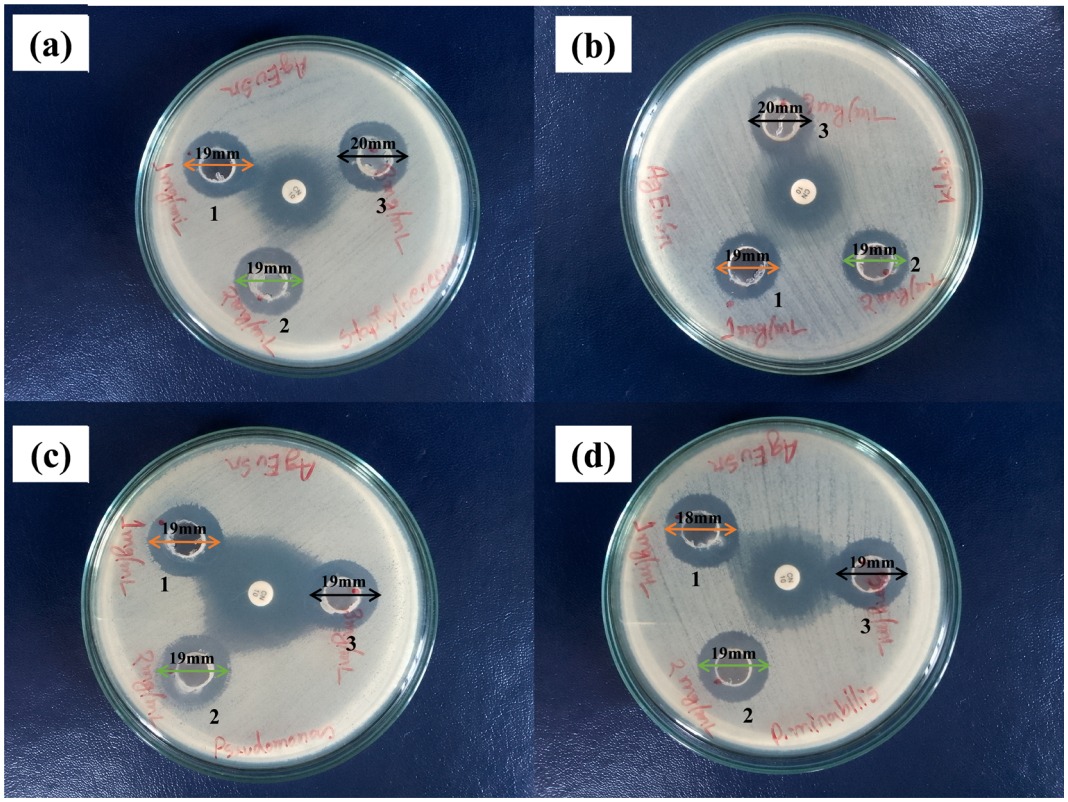

Fig. 11 Antibacterial activities of the $Ag{\cdot}Eu_2O_3{\cdot}SrCO_3$ NMs with different concentrations of solutions, as (1) 1 mg mL^{-1}, (2) 2 mg mL^{-1}, and (3) 3 mg mL^{-1} in the presence of (a) *Staphylococcus aureus*, (b) *Klebsiella pneumonia*, (c) *Pseudomonas aeruginosa*, and (d) *Proteus mirabilis*. (Middle spot is for the control, CN 10).

Nitrite sensor development using $Ag{\cdot}Eu_2O_3{\cdot}SrCO_3$ NMs

Detection of nitrite by LSV study

Concentration variation, pH optimization and scan rate effects. Fig. 12(a) shows a concentration-dependent behavior of the $Ag{\cdot}Eu_2O_3{\cdot}SrCO_3$/Nafion/GCE sensor towards detecting nitrite, as a figure of linear sweep voltammetry (LSV). The existing responses have been depicted as a set of voltammograms at different concentrations of nitrite (between 0.15 and 50 μM). With further increase in concentration, the response level gradually increases, and the highest point of the current is at its highest concentration (50 μM), which shows that there is a direct correlation between the electrochemical current and the concentration of nitrite. This finding can indicate that the $Ag{\cdot}Eu_2O_3{\cdot}SrCO_3$/Nafion/GCE sensor has a sensitive and measurable response to the rise of nitrite concentration in the range of measurements.

The results of Fig. 12(a) are used to construct the calibration curve in Fig. 12(b), where the *x*-axis is the nitrite concentration (in μM), and the *y*-axis is the peak current (μA). The linearity between the response of nitrite and current is seen as the equation of the line was (y = 8.7147x + 80.114), and the correlation coefficient (r^2) was also found to be high (0.975), thus establishing that the relationship between nitrite and current is linear. This calibration curve is another indication of the capability of the $Ag{\cdot}Eu_2O_3{\cdot}SrCO_3$/Nafion/GCE sensor to offer a valid and quantitative determination of the concentration of nitrite within the concentration range under test.

The findings of the pH experiment carried out to measure the effects of different pH levels on the electrochemical sensing of nitrite with a $Ag{\cdot}Eu_2O_3{\cdot}SrCO_3$/Nafion/GCE sensor are presented in Fig. 12(c). Phosphate buffer solutions were used at pH levels of between 5.7 and 8.0. The pH of the medium is important in determining the electrochemical behavior of nitrite and the performance of the sensor. The findings indicate that pH 7.5 gave the highest current, implying that this pH is the best when it comes to detecting nitrite through the electrochemical technique. The current response at lower pH (*e.g.*, 5.7) was lower, probably because the nitrite was protonated or the electrode surface was protonated in the presence of higher levels of protons and thus interfered with the electrochemical reaction. Correspondingly, an increase in the pH value also resulted in a change where the current response declined, which could be explained by the inefficiency of oxidation of nitrite under alkaline conditions. As such, pH 7.5 is determined as the best pH to conduct later electrochemical measurements to obtain the highest sensitivity.

The bar graph in Fig. 12(d) represents the response of the $Ag{\cdot}Eu_2O_3{\cdot}SrCO_3$/Nafion/GCE sensor to detect nitrite by using LSV in the phosphate buffer of pH between 5.7 and 8.0. The maximum value of the current appears at pH = 7.5, which means that the best pH to use in the nitrite electrochemical detection is 7.5. Reduced responses are observed at pH 5.7 and pH 8.0, indicating that these pH values are not the best to use in efficient detection. The responses at pH 6.5 and pH 7.0, although significant, remain lower than the response at pH 7.5, which once again confirms that pH 7.5

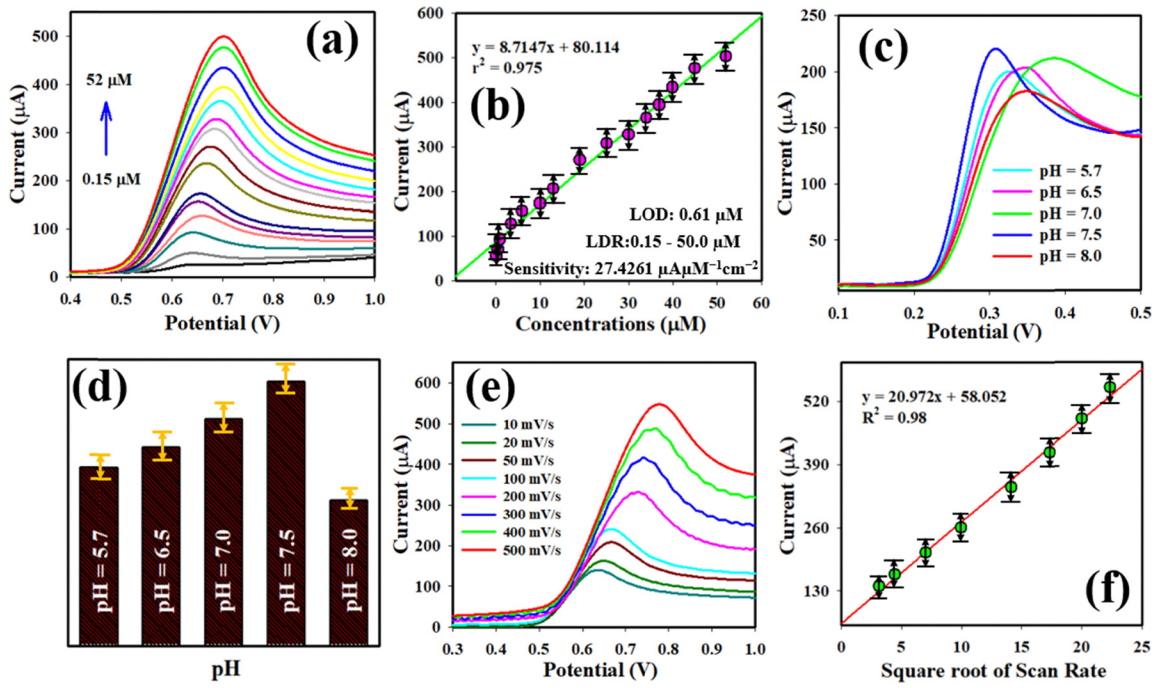

Fig. 12 Electrochemical performance of $Ag{\cdot}Eu_2O_3{\cdot}SrCO_3$/Nafion/GCE: (a) concentration variation response towards nitrite detection by LSV measurements; (b) calibration curve showing the linear relationship between peak current and nitrite concentration; (c) pH optimization study using PBS ranging from 5.7 to 8.0; (d) pH bar diagram showing the highest LSV response at pH 7.5; (e) scan rate effect from 10 to 500 mV s^{-1}; (f) scan rate regression line demonstrating a high value of regression coefficient *i.e.* 0.98.

gives maximum electrochemical performance on nitrite response.

As shown in Fig. 12(e), the procedure of LSV showed a change in the electrochemical response of the Ag·Eu_2O_3·$SrCO_3$/Nafion/GCE sensor to nitrite detection with respect to the scan rate, that is, the linear voltage between 10 mV s^{-1} and 500 mV s^{-1}. The higher the scan rate, the greater the current response, and the maximum current was reached at higher scan rates, which was 500 mV s^{-1}. This trend implies that the electrochemical reaction is scan rate-dependent and implies that higher scan rates can improve the current response of the sensor to nitrite. The trend in the voltammograms indicates the dynamic nature of the electrochemical system, with increasing scan rates indicating the presence of sharper peaks at the increasing scan rate, which represents the rapidity of the kinetics of the nitrite oxidation process.

The plotted regression curve in Fig. 12(f) indicates the following relationship with the peak current as well as the square root of the scan rate: $y = 0.621 + 0.000607x$. The equation ($y = 20.972x + 58.052$) proves that the relationship is linear and the correlation coefficient is very high ($R^2 = 0.98$), which means the relationship is linear. This implies that the electrochemical mechanism of detecting nitrite is diffusion-controlled in nature, with the current proportional to the square root of the scan rate. The linearity also confirms the appropriateness of the Ag·Eu_2O_3·$SrCO_3$/Nafion/GCE in stable and repeatable electrochemical detection of nitrite at different scan rates.

Interference, selectivity, repeatability and reproducibility tests. Fig. 13(a) shows the reaction of the Ag·Eu_2O_3·$SrCO_3$/Nafion/GCE electrode to the various ions, such as nitrite (analyte) and other possible interfering species. A graph is drawn between current (μA) *versus* potential (V) between 0.4 and 0.9 V. The highest value of about 0.7 V is mainly due to the presence of nitrite, which has the greatest current response as compared to other ions. The various ions that are tested, including Ca^{2+}, Ba^{2+}, SO_4^{2-}, HCO_3^-, and K^+, have a different extent of interference, as indicated by the reduced peaks. These findings indicate that although it is possible to be sure of detecting nitrite by this sensor, there is the possibility of interference by other ions, particularly in the higher concentration ranges. The selectivity of the sensor in detecting nitrite

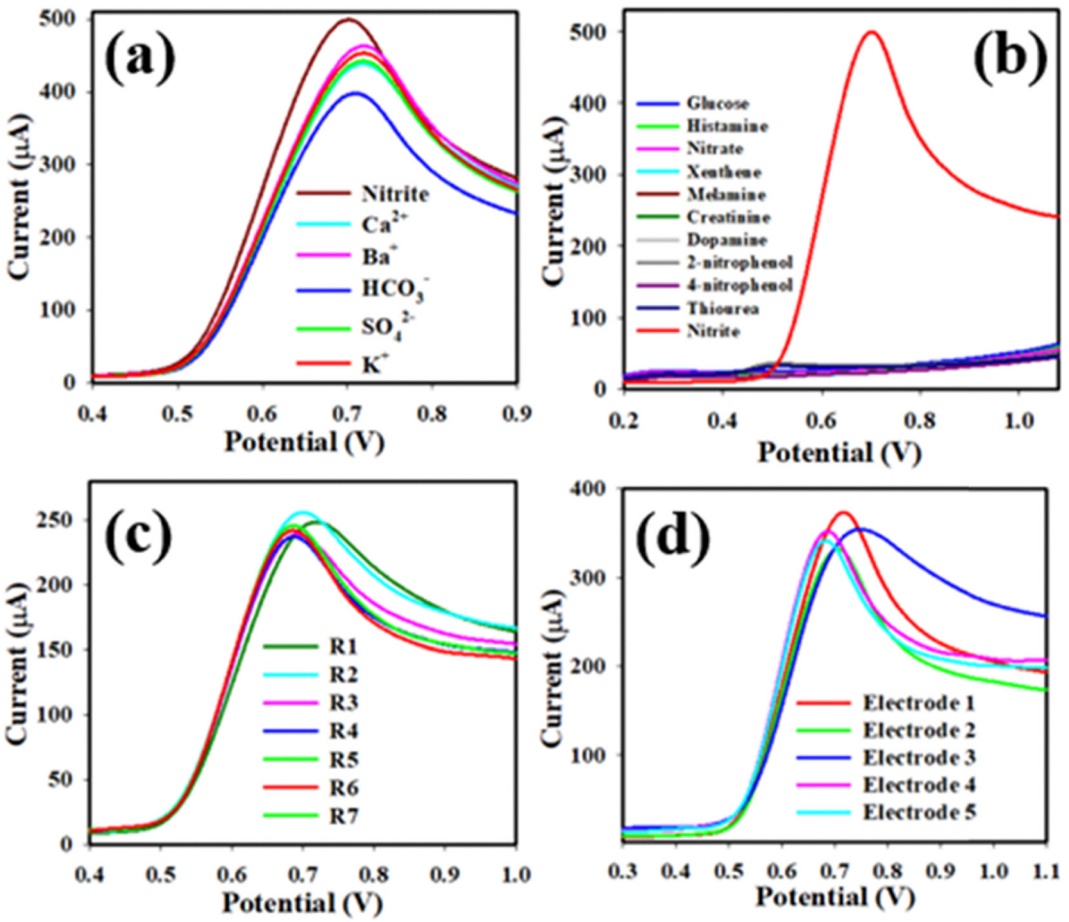

Fig. 13 Electrochemical characterization of Ag·Eu_2O_3·$SrCO_3$/Nafion/GCE: (a) interference study in a nitrite concentration of 50.0 μM, and the nitrite oxidation anodic current was determined with 500–500-fold increase of interfering species. (b) LSV selectivity illustrates the electrode's ability to selectively detect the nitrite in the presence of other species. (c) The LSV response using the same electrode over the course of seven repeated measurements. (d) Response of five prepared electrodes to LSV.

is essential in obtaining the correct measurements of complex samples.

Fig. 13(b) gives further understanding of the specificity of the Ag·Eu_2O_3·$SrCO_3$/Nafion/GCE electrode in the detection of nitrite with respect to the current response of other compounds (glucose, histamine, nitrate, xanthene, and melamine, and creatinine, among others) in the same potential window (0.2–1.0 V). As indicated in the graph, the maximum current generated by nitrite (in red) is much higher than that of the other substances at the electrode, so the electrode has a great selectivity toward nitrite ions. The other compounds, *i.e.*, glucose, histamine, and dopamine, give minimal current signals, implying little interference in the presence of these species. This selectivity is necessary for the practical use of this sensor so that the detection of nitrite can be true even in complex biological or environmental samples where other substances may occur.

Fig. 13(c) demonstrates the test of repeatability of the Ag·Eu_2O_3·$SrCO_3$/Nafion/GCE sensor in the detection of nitrite through the LSV scan rate at 100 mV s^{-1}. The graph shows a couple of voltammograms (R1 to R7), and each curve represents a successive measurement with the same experimental conditions. The results show that the present response of the sensor is very reproducible among repeated usage, and the maximum current has a small variation, which proves that the Ag·Eu_2O_3·$SrCO_3$/Nafion/GCE sensor is reproducible in the detection of nitrite. This consistency implies that the sensor will be consistent in giving similar results when the measurements are repeated, so that the performance of the nitrite electrochemical detector is stable.

Fig. 13(d) shows the reproducibility experiment of newly prepared Ag·Eu_2O_3·$SrCO_3$/Nafion/GCE electrodes to detect nitrite. The voltammograms of five different electrodes (Electrode 1 to Electrode 5) depict comparable currents and potential profiles at the peaks, which means that the newly prepared electrodes demonstrate the similarity in the electrochemical behavior of different samples. The consistency and stability of the fabrication process, indicated by the high degree of similarity in the present responses, can be attributed to the reproducibility of sensor performance, which indicates that the Ag·Eu_2O_3·$SrCO_3$/Nafion/GCE sensor can be recreated at similar levels of success in detecting nitrite.

Electrochemical characterization of the NM fabricated electrode by CV

Conc. variation, control experiment, stability, and scan rate effects. Fig. 14(a) shows the change in the concentration of nitrite during the detection process through cyclic voltammetry (CV) with the Ag·Eu_2O_3·$SrCO_3$/Nafion/GCE electrode. Cyclic voltammograms were obtained in diverse concentrations of nitrite, of 0.15 μM to 50.0 μM. The current response is increased significantly with an increase in the concentration of nitrite. The applied potential is plotted on the *x*-axis and the current measured is plotted on the *y*-axis in μA. These data show that there is a definite tendency, as the present response is directly proportional to the concentration of nitrite, which means that the electrochemical signal is linearly dependent on the concentration of nitrite. The behavior shows that the electrode has the potential of detecting nitrite over a broad concentration range, and the lower limit of detection is low. The improved current response is an indication of higher electrochemical activity brought about by the interaction between the electrode and the nitrite ions, indicating that the sensor is very sensitive and can be used to detect nitrite quantitatively.

Fig. 14(b) shows a control experiment, with the electrochemical activities of the bare/GCE as well as coated Ag·Eu_2O_3·$SrCO_3$/Nafion/GCE electrodes in the presence and absence of nitrite as measured by cyclic voltammetry. The cyclic voltammograms indicate that the unmodified bare/GCE electrode has a normal response and that in the uncoated GCE (Ag·Eu_2O_3·$SrCO_3$ coated without nitrite) the redox peak shifts, which indicates that there was a better electrochemical interface because of the coating. Inclusion of nitrite leads to a very high response of current when it is introduced (coated with nitrite), and this indicates the high affinity between the ions of nitrite and the Ag·Eu_2O_3·$SrCO_3$ coating. Such an improvement in current indicates that the Ag·Eu_2O_3·$SrCO_3$/Nafion/GCE electrode is very sensitive to nitrite, and it can be used to selectively and sensitively detect nitrite. The comparison has brought to the fore the use of the coating in improving the electrochemical characteristics of the electrode in the detection of nitrite. High surface area from the morphology of Eu_2O_3/$SrCO_3$, the specific catalytic activity of Eu_2O_3 (Eu_2O_3 provides oxygen vacancies that contribute to adsorption and activation of nitrite), and the high conductivity of Ag all contributed to the nitrite oxidation synergistically.

The cyclic voltammogram (CV) in Fig. 14(c) shows the stability of the Ag·Eu_2O_3·$SrCO_3$/Nafion/GCE electrode, tested at 50 cycles at a scan rate of 100 mV s^{-1}. This cyclic nature is observed with the typical peaks (oxidation and reduction), which are associated with the electrochemical functionality of the Ag·Eu_2O_3·$SrCO_3$/Nafion/GCE electrode in ferro/ferricyanide couples. The fact that no substantial alterations are observed in the shape and location of the peaks once the 50 cycles are completed shows that the fabricated electrode can be considered stable and electrochemically active. This is an indication that the Ag·Eu_2O_3·$SrCO_3$/Nafion/GCE electrode is well cyclically stable in the given experimental conditions, and thus it may be used in the long run when used in electrochemical sensing. The electrochemical response is unaffected, and there is no visible decomposition of the substance or any change in the electrochemical characteristics of the substance during 50 cycling.

The scan rate variation study of the Ag·Eu_2O_3·$SrCO_3$/Nafion/GCE electrode is shown in Fig. 14(d) in which cyclic voltammetry of the electrode was conducted across a scan rate of 10 mV s^{-1} to 500 mV s^{-1}. The graph shows the relationship between current (μA) and potential (V) at the various scan rates, indicating that the current of action rises as the scan rates rise. This current growth is associated with the accelerated electrochemical activity and improved charge transfer in high scan rates. The trend observed indicates that the electrochemical

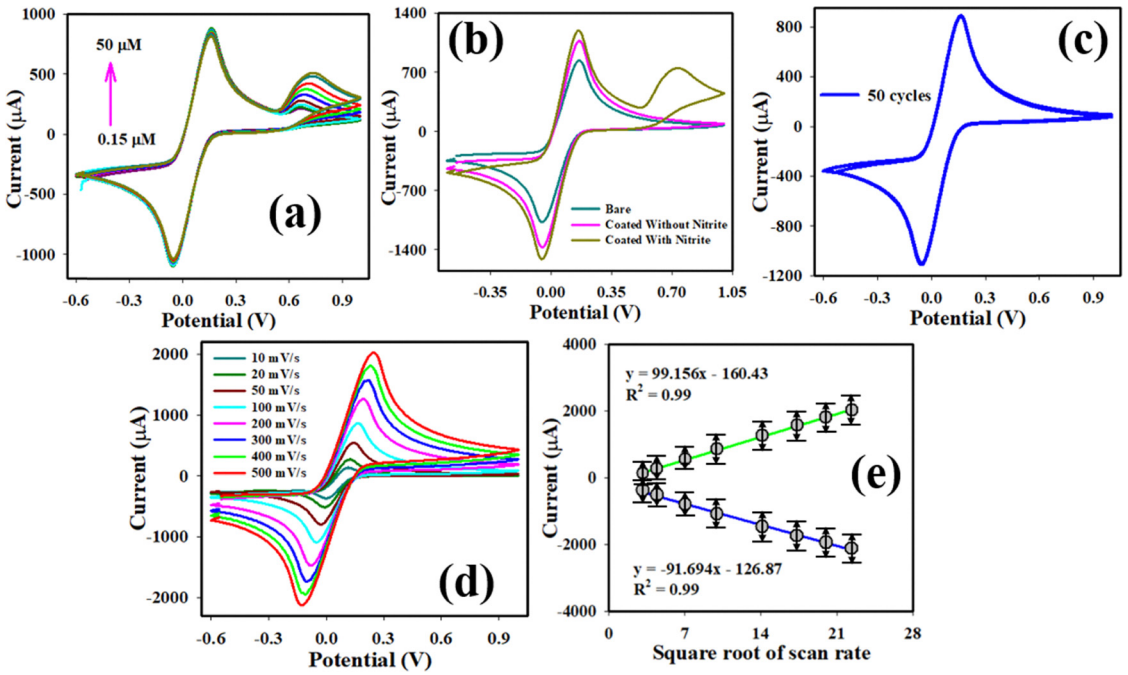

Fig. 14 (a) CV demonstrating concentration variations from 0.15 to 50 μM, representing the sensitivity and detection ability of Ag·Eu_2O_3·$SrCO_3$/Nafion/GCE towards nitrite; (b) control experiment for comparison of the bare/GCE and coated Ag·Eu_2O_3·$SrCO_3$/Nafion/GCE response; (c) stability test of Ag·Eu_2O_3·$SrCO_3$/Nafion/GCE at a scan rate of 100 mV s^{-1} for 50 cycles; (d) scan rate analysis (10 to 500 mV s^{-1}), providing understanding of the kinetics of the electrochemical process; and (e) regression line for scan rate data.

properties of the Ag·Eu_2O_3·$SrCO_3$/Nafion/GCE electrode are scan rate-dependent and the electrode has a distinct peak current which is directly proportional to the variation in the scan rate.

Fig. 14(e) shows the scan rate variation data, and Fig. 14(d) shows the regression. The current (μA) *vs.* the square root of scan rate (mV s^{-1}) plot indicates a linear relationship that is typical of a diffusion-controlled electrochemical process. The linear dependence is also supported by the large coefficient of correlation (R^2 = 0.99) of both anodic and cathodic currents, which means that the electrochemical reaction at the Ag·Eu_2O_3·$SrCO_3$/Nafion/GCE electrode is governed by diffusion. This kind of outcome shows the consistency of the electrode in nitrite detection and indicates the consistency of the electrochemical behavior at varying scan rates. The analysis of regression gives a quantitative foundation to the analysis of the mechanism of electrochemical reaction and diffusion taking place. The comparative performances of this newly fabricated electrode in nitrite detection with various nanostructure materials using electrochemical approach have presented in the Table 2.

Validation of the sensor with real sample analysis. The nitrite level was determined in three waters of the region, and the fact that no trace of nitrite was present, or the amount of the level was lower than the detection limit, probably led to the fact that no measurements of nitrite were obtained at the first steps of the experiment. The traditional method of addition was used to determine the quantity of nitrite accurately. The findings can show that Ag·Eu_2O_3·$SrCO_3$/Nafion/GCE sensors are sensitive and selective, which are able to detect nitrite in different water matrices. The sensor is very sensitive and is therefore effective in environmental monitoring applications. Table 3 reflects the result of the actual analysis of the real sample, which was conducted based on LSV. The recovery rates were between 97% and 98, indicating high accuracy and reliability of the method. The results specify that this approach is effective and reliable in the determination of nitrite in environmental samples. Also, the analysis ensured that there was very little interference with other substances that were found in the water samples, hence supporting the strength of the method in real-world applications.

Table 2 Comparative evaluation of the new Ag·Eu_2O_3·$SrCO_3$/Nafion/GCE sensor against previous nitrite sensors

Modified electrodes	Technique	LOD (μM)	Linear range	Sensitivity (μA μM^{-1} cm^{-2})	Ref.
GO@Fe_2O_3/Y_2O_3 NCs	LSV	2.24 mM	0.74–1.09 M	7.383	90
CS-NMO/GCE	SWV	0.19	0.96–1080 μM	—	31
Y/BaO-fMWCNT/GCE	DPV	0.297	1 nM–1.29 mM	9.30	91
CB-PLA	DPV	1.8	5.0–500.0	—	29
PANI/AC@Ag_3PO_4/GCE	LSV	0.21	1–15	7.595	92
Ag·Eu_2O_3·$SrCO_3$/Nafion/GCE	LSV	0.61	0.15–50 μM	27.4261	This Work

Table 3 Analysis of spiked real samples for nitrite detection using the Ag·Eu_2O_3·$SrCO_3$/Nafion/GCE electrochemical sensor

Real sample	Added nitrite (μM)	Determination of nitrite conc. by Ag·Eu_2O_3·$SrCO_3$/Nafion/GCE (μM)			Average recovery	RSD (%) (n = 3)
		R1	R2	R3		
Sea water	50	50.0	48.5	49.0	98.3	1.55
Tap water	50	49.8	47.0	49.5	97.5	3.15
Industrial water	50	49.7	50.0	48.0	98.5	2.19

Conclusions

Finally, the Ag·Eu_2O_3·$SrCO_3$ NMs were synthesized using a facile, inexpensive, co-precipitation approach. The NMs were characterized using XRD, SEM, EDS, FTIR, Raman, and PL. By degrading CV dye, we examined the photocatalytic activity of the NMs using a variety of factors, including contact time, pH influence, catalyst reusability, and catalytic doses. Between 0.05 and 0.07 g of NMs, 0.06 g resulted in better degradation at pH 9.2 (97.7%; dye removal efficiency) and eliminated half of the dye within 26 min. Furthermore, the NMs showed high photocatalytic activity at pH 9.2 rather than pH 4 or 7. The produced NMs also showed outstanding reusability, losing only 11.03% of their effectiveness after four reuses. Additionally, after an hour of stirring in the dark, 0.06 g of adsorbent showed good dye adsorption ability in a basic solution (13.433% of dye adsorbed with an adsorption capacity of 112 mg g^{-1}). During photocatalysis, we detected hydroxyl radicals ($^{\bullet}OH$), which are responsible for dye degradation. Exposure to visible light boosted the generation of the $^{\bullet}OH$ radical over time. The higher generation of radicals in a basic medium, as compared to an acidic or neutral one, supported the enhanced photocatalytic activity. Furthermore, it was shown that the NMs were capable of inhibiting both Gram-positive and Gram-negative bacteria. Finally, an electrochemical sensor that efficiently detected nitrite with good sensitivity was developed using a Ag·Eu_2O_3·$SrCO_3$ NM-modified GCE with 5% Nafion by means of the drop-cast method. The NMs possess very high electrical conductivity, so agglomeration is undesirable, and a uniform electrode interface is formed. The Ag·Eu_2O_3·$SrCO_3$/Nafion/GCE sensor has a linear response to the detection of nitrite in the concentration range between 0.15 and 50 μM, and the detection limit is 0.61 μM. In addition, the sensor exhibited high anti-interference characteristics. It was observed that the NM-fabricated sensor was practically valid by LSV in the detection of nitrite in water samples collected from different sources.

Conflicts of interest

There are no conflicts to declare.

Data availability

The data supporting this article have been included as part of the supplementary information (SI). Supplementary information is available. See DOI: https://doi.org/10.1039/d6ma00143b.

Acknowledgements

Md Abdus Subhan acknowledges a SUST Research Grant (No. PS/2022/1/09). He also acknowledges his current affiliation with Texas Tech University, Lubbock, Texas, for their support. This project was also funded by the Deanship of Scientific Research (DSR) at King Abdulaziz University, Jeddah, Saudi Arabia, under grant no. (IPP: 48-961-2025). The authors, therefore, acknowledge with thanks DSR for technical and financial support.

References

1 S. Yadav, K. Shakya, A. Gupta, D. Singh, A. R. Chandran, A. V. Aanappalli, K. Goyal and N. Rani, Kalawati Saini, *Environ. Sci. Pollut. Res.*, 2023, **30**, 71912–71932, DOI: 10.1007/s11356-022-20818-6.
2 K. Yamjala, M. S. Nainar and N. R. Ramisetti, *Food Chem.*, 2016, **192**, 813–824, DOI: 10.1016/j.foodchem.2015.07.085.
3 E. Guerra, M. Llompart and C. Garcia-Jares, *Cosmet*, 2018, **5**, 47, DOI: 10.3390/cosmetics5030047.
4 M. Wainwright, *Dyes Pigm.*, 2008, **76**, 582–589, DOI: 10.1016/j.dyepig.2007.01.015.
5 M. Wainwright, *Biotech. Histochem.*, 2003, **78**, 147–155, DOI: 10.1080/10520290310001602404.
6 S. Nair, B. Manu and A. Azhoni, *J. Environ. Manage.*, 2021, **296**, 113105, DOI: 10.1016/j.jenvman.2021.113105.
7 L. Van der Schueren and K. De Clerck, *Text. Res. J.*, 2010, **80**, 590–603, DOI: 10.1177/0040517509346443.
8 T. A. Khattab, M. S. Abdelrahman and M. Rehan, *Environ. Sci. Pollut. Res.*, 2020, **27**, 3803–3818, DOI: 10.1007/s11356-019-07137-z.
9 G. Thennarasu, S. Rajendran, A. Kalairaj, H. S. Rathore, R. C. Panda and T. Senthilvelan, *Clean Technol. Environ.*, 2025, **27**, 495–516, DOI: 10.1007/s10098-024-02960-6.
10 M. Sifat, E. Shin, A. Schevon, H. Ramos, A. Pophali, H. J. Jung, G. Halada, Y. Meng, N. Olynik and D. J. Sprouster, *Catal.*, 2024, **14**, 377, DOI: 10.3390/catal14060377.
11 J. P. Shubha, S. F. Adil, M. Khan, M. R. Hatshan and A. Khan, *ACS Omega*, 2021, **6**, 3866–3874, DOI: 10.1021/acsomega.0c05670.
12 D. A. Kader, *RSC Adv.*, 2023, **13**, 34904–34915, DOI: 10.1039/D3RA06448D.
13 M. K. Debanath and S. Karmakar, *Mater. Lett.*, 2013, **111**, 116–119, DOI: 10.1016/j.matlet.2013.08.069.
14 T. N. Q. Trang, T. B. Phan, N. D. Nam and V. T. H. Thu, *ACS Appl. Mater. Interfaces*, 2020, **12**, 12195–12206, DOI: 10.1021/acsami.9b15578.

15 Y. Chen, C. Shen, J. Wang, G. Xiao and G. Luo, *ACS Sustainable Chem. Eng.*, 2018, **6**, 13276–13286, DOI: 10.1021/acssuschemeng.8b02860.
16 S. Tang and J. Zheng, *Adv. Healthcare Mater.*, 2018, **7**, 1701503, DOI: 10.1002/adhm.201701503.
17 T. Hadamek, S. Rangan, J. Viereck, D. Shin, A. B. Posadas, R. A. Bartynski and A. A. Demkov, *J. Appl. Phys.*, 2020, **127**, 074101, DOI: 10.1063/1.5139227.
18 R. Padmanabhan, N. Bhat and S. Mohan, *IEEE Trans. Electron Devices*, 2012, **59**, 1364–1370, DOI: 10.1109/TED.2012.2188329.
19 X. Li, G. Lu, Y. Guo, Y. Guo, Y. Wang, Z. Zhang, X. Liu and Y. Wang, *Catal. Commun.*, 2007, **8**, 1969–1972, DOI: 10.1016/j.catcom.2007.03.013.
20 T. H. AlAbdulaal, V. Ganesh, M. AlShadidi, M. S. A. Hussien, A. Bouzidi, H. Algarni, H. Y. Zahran, M. S. Abdel-wahab, I. S. Yahia and S. Nasr, *Mater.*, 2022, **15**, 3257, DOI: 10.3390/ma15093257.
21 W. S. Mohamed and A. M. Abu-Dief, *J. Phys. Chem. Solids*, 2018, **116**, 375–385, DOI: 10.1016/j.jpcs.2018.02.008.
22 J. P. Shubha, H. S. Savitha, S. F. Adil, M. Khan, M. R. Hatshan, K. Kavalli and B. Shaik, *Molecules*, 2021, **26**, 4661, DOI: 10.3390/molecules26154661.
23 S. Ni, X. Yang and T. Li, *Mater. Lett.*, 2011, **65**, 766–768, DOI: 10.1016/j.matlet.2010.11.056.
24 W. Y. Qian, D. M. Sun, R. R. Zhu, X. L. Du, H. Liu and S. L. Wang, *Int. J. Nanomed.*, 2012, **7**, 5781–5792, DOI: 10.2147/IJN.S34773.
25 P. Lu, X. Hu, Y. Li, M. Zhang, X. Liu, Y. He, F. Dong, M. Fu and Z. Zhang, *RSC Adv.*, 2018, **8**, 6315–6325, DOI: 10.1039/C7RA11565B.
26 G. E. Hernández-Villegas, W. J. Pech-Rodríguez, G. G. Suarez-Velázquez and C. A. Calles-Arriaga, *Emergent Mater.*, 2025, 1–15, DOI: 10.1007/s42247-025-01185-7.
27 K. Singh, A. Mishra, D. Sharma and K. Singh, *Appl. Targeted Nano Drugs Delivery Syst.*, 2019, 343–356, DOI: 10.1016/B978-0-12-814029-1.00013-2.
28 D. Wang, L. Zhao, H. Ma, H. Zhang and L. H. Guo, *Environ. Sci. Technol.*, 2017, **51**, 10137–10145, DOI: 10.1021/acs.est.7b00473.
29 L. R. G. Silva, D. R. Santos-Neto, J. S. Stefano, D. H. de Oliveira, L. S. da Silva, H. S. Pittner, C. L. Handa, R. A. A. Muñoz and D. P. Rocha, *Talanta Open*, 2025, **11**, 100443, DOI: 10.1016/j.talo.2025.100443.
30 W. Wichitnithad, S. Nantaphol, K. Noppakhunsomboon and P. Rojsitthisak, *Saudi Pharm. J.*, 2023, **31**, 295–311, DOI: 10.1016/j.jsps.2022.12.010.
31 E. Ahmadi, F. Azarm, M. Mahdavijalal and A. Akbari, *Electrochim. Acta*, 2025, **542**, 147379, DOI: 10.1016/j.electacta.2025.147379.
32 A. Ferlazzo, V. Bressi, C. Espro, D. Iannazzo, E. Piperopoulos and G. Neri, *J. Electroanal. Chem.*, 2023, **928**, 117071, DOI: 10.1016/j.jelechem.2022.117071.
33 R. Lucchetti, L. Onotri, L. Clarizia, F. Di Natale, I. Di Somma, R. Andreozzi and R. Marotta, *Appl. Catal., B*, 2017, **202**, 539–549, DOI: 10.1016/j.apcatb.2016.09.043.
34 M. Jannat, R. Fatimah and M. Kishida, *Biochem. Biophys. Res. Commun.*, 2014, **452**, 608–613, DOI: 10.1016/j.bbrc.2014.08.114.
35 N. S. Bryan, D. D. Alexander, J. R. Coughlin, A. L. Milkowski and P. Boffetta, *Food Chem. Toxicol.*, 2012, **50**, 3646–3665, DOI: 10.1016/j.fct.2012.07.062.
36 L. Cui, J. Zhu, X. Meng, H. Yin, X. Pan and S. Ai, *Sens. Actuators, B*, 2012, **161**, 641–647, DOI: 10.1016/j.snb.2011.10.083.
37 P. Miao, M. Shen, L. Ning, G. Chen and Y. Yin, *Anal. Bioanal. Chem.*, 2011, **399**, 2407–2411, DOI: 10.1007/s00216-010-4642-3.
38 Z. Chen, Y. Zhang, J. Zhang and J. Zhou, *J. Electrochem. Soc.*, 2019, **166**, B787, DOI: 10.1149/2.1111910jes.
39 J. K. F. van Staden, R. G. Nuta and G. L. Tatu, *J. Electrochem. Soc.*, 2018, **165**, B565, DOI: 10.1149/2.0311813jes.
40 World Health Organization, (No. WHO/SDE/WSH/04.03/56) (2003).
41 A. C. M. Oliveira, E. Bernalte, L. M. A. Melo, K. K. L. Augusto, W. T. P. dos Santos, O. Fatibello-Filho, R. A. A. Muñoz, R. D. Crapnell and C. E. Banks, *Microchem. J.*, 2025, **218**, 115553, DOI: 10.1016/j.microc.2025.115553.
42 U. Shahzad, H. M. Marwani, M. F. Rabbee, S. Y. Alfaifi, K. A. Alzahrani, M. M. R. Khan and M. M. Rahman, *Mater. Chem. Phys.*, 2024, **328**, 130000, DOI: 10.1016/j.matchemphys.2024.130000.
43 H. Kodamatani, S. Yamazaki, K. Saito, T. Tomiyasu and Y. Komatsu, *J. Chromatogr. A*, 2009, **1216**, 3163–3167, DOI: 10.1016/j.chroma.2009.01.096.
44 K. M. Miranda, M. G. Espey and D. A. Wink, *Nitric oxide*, 2001, **5**, 62–71, DOI: 10.1006/niox.2000.0319.
45 Z. Zhao, J. Zhang, W. Wang, Y. Sun, P. Li, J. Hu, L. Chen and W. Gong, *Appl. Surf. Sci.*, 2019, **485**, 274–282, DOI: 10.1016/j.apsusc.2019.04.202.
46 H. Essousi, H. Barhoumi, M. Bibani, N. Ktari, F. Wendler, A. Al-Hamry and O. Kanoun, *J. Sens.*, 2019, **2019**, 4257125, DOI: 10.1155/2019/4257125.
47 U. Shahzad, M. Saeed, H. M. Marwani, J. Y. Al-Humaidi, S. U. Rehman, R. H. Althomali, M. R. Awual and M. M. Rahman, *Crit. Rev. Anal. Chem.*, 2025, **55**, 1081–1098, DOI: 10.1080/10408347.2024.2337876.
48 S. Nasraoui, A. Al-Hamry, P. R. Teixeira, S. Ameur, L. G. Paterno, M. B. Ali and O. Kanoun, *J. Electroanal. Chem.*, 2021, **880**, 114893, DOI: 10.1016/j.jelechem.2020.114893.
49 T. A. Sheikh, M. Ismail, M. F. Rabbee, H. Khan, A. Rafique, Z. Rasheed, A. Siddique, M. Z. Rafiq, Z. A. K. Khattak, S. M. S. Jillani, U. Shahzad, M. N. Akhtar, M. Saeed, K. A. Alzahrani, J. Uddin, M. M. Rahman and F. Verpoort, *Crit. Rev. Anal. Chem.*, 2024, **55**, 1621–1666, DOI: 10.1080/10408347.2024.2379851.
50 J. Zhang, T. Zhang and J. H. Yang, *Ionics*, 2022, **28**, 2041–2064, DOI: 10.1007/s11581-022-04509-3.
51 P. Ptáček, E. Bartoníčková, J. Švec, T. Opravil, F. Šoukal and F. Frajkorová, *Ceram. Int.*, 2015, **41**, 115–126, DOI: 10.1016/j.ceramint.2014.08.043.
52 L. Ye, J. Liu, Z. Jiang, T. Peng and L. Zan, *Appl. Catal., B*, 2013, **142–143**, 1–7, DOI: 10.1016/j.apcatb.2013.04.058.

53 K. A. Sultana, M. T. Islam, J. A. Silva, R. S. Turley, J. A. Hernandez-Viezcas, J. L. Gardea-Torresdey and J. C. Noveron, *J. Mol. Liq.*, 2020, **307**, 112931, DOI: 10.1016/j.molliq.2020.112931.
54 D. P. Padiyan, A. Marikani and K. R. Murali, *Mater. Chem. Phys.*, 2003, **78**, 51–58, DOI: 10.1016/S0254-0584(02)00211-0.
55 W. S. Mohamed, M. F. Hasaneen and E. K. Shokr, *Mater. Res. Express*, 2017, **4**, 046406, DOI: 10.1088/2053-1591/aa6b7b.
56 Q. Huang, C. Wang and Q. Shan, *Nanomaterials*, 2022, **12**, 2320, DOI: 10.3390/nano12142320.
57 H. E. A. Mohamed, K. Hkiri, M. Khenfouch, S. Dhlamini, M. Henini and M. Maaza, *J. Opt. Soc. Am. A*, 2020, **37**, C73–C79, DOI: 10.1364/JOSAA.396244.
58 T. Thongtem, N. Tipcompor, A. Phuruangrat and S. Thongtem, *Mater. Lett.*, 2010, **64**, 510–512, DOI: 10.1016/j.matlet.2009.11.060.
59 M. Rahimi-Nasrabadi, S. M. Pourmortazavi, M. Sadeghpour Karimi, M. Aghazadeh, M. R. Ganjali and P. Norouzi, *J. Mater. Sci.: Mater. Electron.*, 2017, **28**, 13267–13277, DOI: 10.1007/s10854-017-7161-6.
60 M. A. Subhan, N. Uddin, P. Sarker, A. K. Azad and K. Begum, *Spectrochim. Acta, Part A*, 2015, **149**, 839–850, DOI: 10.1016/j.saa.2015.05.024.
61 S. Kumar, R. Prakash and V. Singh, *Rev. Adv. Sci. Eng.*, 2016, **4**, 247–257, DOI: 10.1166/rase.2015.1102.
62 C. B. Annapurna Devi, S. Mahamuda, K. Swapna, M. Venkateswarlu, A. Srinivasa Rao and G. Vijaya Prakash, *Opt. Mater.*, 2017, **73**, 260–267, DOI: 10.1016/j.optmat.2017.08.010.
63 M. A. Subhan, P. C. Saha, M. A. Hossain, M. M. Alam, A. M. Asiri, M. M. Rahman, M. Al-Mamun, T. P. Rifat, T. Raihan and A. K. Azad, *RSC Adv.*, 2020, **10**, 30603–30619, DOI: 10.1039/D0RA05008C.
64 A. Divya, T. Mathavan, S. Harish, J. Archana, A. M. F. Benial, Y. Hayakawa and M. Navaneethan, *Appl. Surf. Sci.*, 2019, **487**, 1271–1278, DOI: 10.1016/j.apsusc.2019.04.173.
65 P. Filipczak, K. Halagan, J. Ulański and M. Kozanecki, *Beilstein J. Nanotechnol.*, 2021, **12**, 497–506, DOI: 10.3762/bjnano.12.40.
66 G. A. Haghighat, G. B. Gholikandi, M. Mirabi and M. Shams, *J. Photochem. Photobiol., A*, 2024, **449**, 115342, DOI: 10.1016/j.jphotochem.2023.115342.
67 R. Dhanabal and P. G. Priya, *Mater. Sci. Semicond. Process.*, 2025, **192**, 109481, DOI: 10.1016/j.mssp.2025.109481.
68 S. Ramanathan, R. M. Rashmitha, H. C. Chuang, J. Kasemchainan, M. K. Arumugam, I. S. Lydia, S. Pandiyarajan and S. Poompradub, *Process Saf. Environ. Prot.*, 2024, **187**, 145–158, DOI: 10.1016/j.psep.2024.04.096.
69 A. T. Brandão, S. Rosoiu-State, R. Costa, L. B. Enache, G. V. Mihai, J. A. Vazquez, J. Valcarcel, L. Anicai, M. Enachescu and C. M. Pereira, *J. Water Proc. Eng.*, 2025, **71**, 107288, DOI: 10.1016/j.jwpe.2025.107288.
70 M. T. Yassin, F. O. Al-Otibi and A. A. Al-Askar, *Separations*, 2023, **10**, 513, DOI: 10.3390/separations10090513.
71 S. E. Elashery, I. Ibrahim, H. Gomaa, M. M. El-Bouraie, I. A. Moneam, S. S. Fekry and G. G. Mohamed, *Magnetochemistry*, 2023, **9**, 56, DOI: 10.3390/magnetochemistry9020056.
72 S. G. Divakara, B. Mahesh, B. K. Jayanna and H. G. Anil Kumar, *Green Chem. Lett. Rev.*, 2025, **18**, 2543931, DOI: 10.1080/17518253.2025.2543931.
73 K. Dharmalingam, A. K. Bojarajan, R. Gopal, E. Thangavel, S. A. Burhan Al Omari and S. Sangaraju, *Sci. Rep.*, 2024, **14**, 14518, DOI: 10.1038/s41598-024-65163-5.
74 S. Mohebali, D. Bastani and H. Shayesteh, *J. Mol. Struct.*, 2019, **1176**, 181–193, DOI: 10.1016/j.molstruc.2018.08.068.
75 L. Mouni, L. Belkhiri, J. C. Bollinger, A. Bouzaza, A. Assadi, A. Tirri, F. Dahmoune, K. Madani and H. Remini, *Appl. Clay Sci.*, 2018, **153**, 38–45, DOI: 10.1016/j.clay.2017.11.034.
76 T. A. Aragaw and A. N. Alene, *Emerging Contam.*, 2022, **8**, 59–74, DOI: 10.1016/j.emcon.2022.01.002.
77 M. Saidi, B. A. Reguig, M. El Amine Monir, T. M. Althagafi, M. Fatmi, A. Remil, A. Zehhaf and M. A. Ghebouli, *Sci. Rep.*, 2025, **15**, 21991, DOI: 10.1038/s41598-025-05787-3.
78 R. K. Sharma, S. Yadav, S. Dutta, H. B. Kale, I. R. Warkad, R. Zbořil, R. S. Varma and M. B. Gawande, *Chem. Soc. Rev.*, 2021, **50**, 11293–11380, DOI: 10.1039/D0CS00912A.
79 A. M. Shawky, R. Elshypany, H. M. El Sharkawy, M. F. Mubarak and H. Selim, *Sci. Rep.*, 2024, **14**, 2456, DOI: 10.1038/s41598-024-52454-0.
80 Y. Zheng, J. Lin and Q. Wang, *Photochem. Photobiol. Sci.*, 2012, **11**, 1567–1574, DOI: 10.1039/c2pp25184a.
81 S. Bano, N. Ahmad, S. Sultana, S. Sabir and M. Z. Khan, *J. Environ. Chem. Eng.*, 2019, **7**, 103012, DOI: 10.1016/j.jece.2019.103012.
82 M. A. Subhan, T. P. Rifat, P. C. Saha, M. M. Alam, A. M. Asiri, T. Raihan, A. K. Azad, W. Ghann, J. Uddin and M. M. Rahman, *New J. Chem.*, 2021, **45**, 1634–1650, DOI: 10.1039/D0NJ04813E.
83 L. Wang, J. Ge, A. Wang, M. Deng, X. Wang, S. Bai, R. Li, J. Jiang, Q. Zhang, Y. Luo and Y. Xiong, *Angew. Chem.*, 2014, **126**, 5207–5211, DOI: 10.1002/ange.201310635.
84 Z. Yang, X. Xu, X. Liang, C. Lei, Y. Cui, W. Wu, Y. Yang, Z. Zhang and Z. Lei, *Appl. Catal., B*, 2017, **205**, 42–54, DOI: 10.1016/j.apcatb.2016.12.012.
85 Y. Zhang, C. Wang, A. Cai, R. Yin, X. Yuan, H. Kang, Q. Chen, Y. Song, H. Guo and H. Yin, *Appl. Surf. Sci.*, 2023, **635**, 157714, DOI: 10.1016/j.apsusc.2023.157714.
86 X. He, J. Ouyang and H. Yang, *RSC Adv.*, 2013, **3**, 20385–20390, DOI: 10.1039/C3RA42701C.
87 N. Talebian, S. M. Amininezhad and M. Doudi, *J. Photochem. Photobiol., B*, 2013, **120**, 66–73, DOI: 10.1016/j.jphotobiol.2013.01.004.
88 H. A. Foster, I. B. Ditta, S. Varghese and A. Steele, *Appl. Microbiol. Biotechnol.*, 2011, **90**, 1847–1868, DOI: 10.1007/s00253-011-3213-7.
89 R. K. Dutta, B. P. Nenavathu, M. K. Gangishetty and A. V. R. Reddy, *Colloids Surf., B*, 2012, **94**, 143–150, DOI: 10.1016/j.colsurfb.2012.01.046.
90 M. Saeed, H. M. Marwani, M. Shalauddin, S. Y. Alfaifi, S. Akhter, K. A. Alzahrani, W. J. Basirun and M. M. Rahman, *J. Ind. Eng. Chem.*, 2025, **144**, 552–564, DOI: 10.1016/j.jiec.2024.09.054.

91 U. Shahzad, A. N. Alotaibi, H. M. Marwani, M. A. J. Mazumder, A. Al-Dakhil, A. E. Alsafrani, A. Albishri and M. M. Rahman, *Microchem. J.*, 2025, **215**, 114536, DOI: 10.1016/j.microc.2025.114536.

92 B. Chemseddin, U. Shahzad, T. Asma, J. Y. Al-Humaidi, A. Mahieddine, K. A. Alzahrani, M. Ifires and M. M. Rahman, *J. Ind. Eng. Chem.*, 2025, **156**, 842–853, DOI: 10.1016/j.jiec.2025.09.026.